# Pattern recognition in the nucleation kinetics of non-equilibrium self-assembly

Constantine Glen Evans[1,2,3], Jackson O'Brien[4], Erik Winfree[1], Arvind Murugan[4]

[1]*California Institute of Technology, Pasadena, CA,* [2]*Evans Foundation for Molecular Medicine, Pasadena, CA,* [3]*Maynooth University, Maynooth, Ireland,* [4]*University of Chicago, Chicago, IL*

**Inspired by biology's most sophisticated computer, the brain, neural networks constitute a profound reformulation of computational principles. Remarkably, analogous high-dimensional, highly-interconnected computational architectures also arise within information-processing molecular systems inside living cells, such as signal transduction cascades and genetic regulatory networks. Might neuromorphic collective modes be found more broadly in other physical and chemical processes, even those that ostensibly play non-information-processing roles such as protein synthesis, metabolism, or structural self-assembly? Here we examine nucleation during self-assembly of multicomponent structures, showing that high-dimensional patterns of concentrations can be discriminated and classified in a manner similar to neural network computation. Specifically, we design a set of 917 DNA tiles that can self-assemble in three alternative ways such that competitive nucleation depends sensitively on the extent of co-localization of high-concentration tiles within the three structures. The system was trained in-silico to classify a set of 18 grayscale 30×30 pixel images into three categories. Experimentally, fluorescence and atomic force microscopy monitoring during and after a 150-hour anneal established that all trained images were correctly classified, while a test set of image variations probed the robustness of the results. While slow compared to prior biochemical neural networks, our approach is surprisingly compact, robust, and scalable. This success suggests that ubiquitous physical phenomena, such as nucleation, may hold powerful information processing capabilities when scaled up as high-dimensional multicomponent systems.**

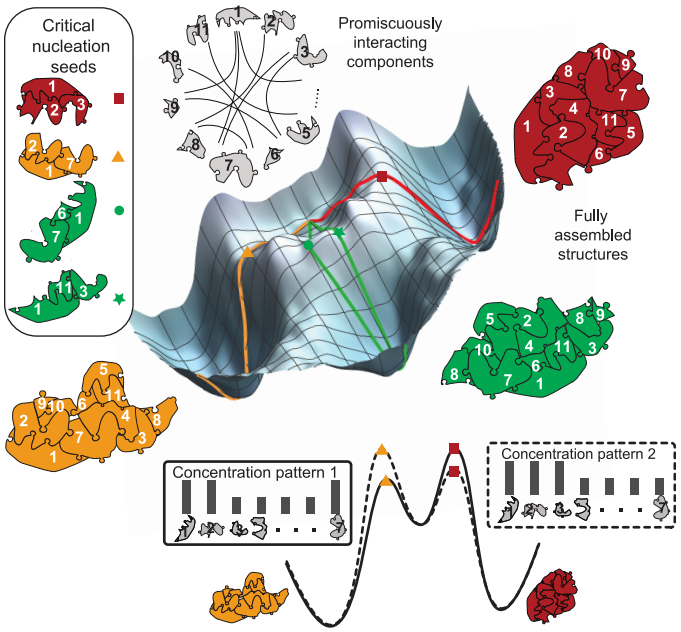


**Fig. 1 | Conceptual framework for pattern recognition by nucleation.** When one set of molecules can potentially assemble multiple distinct structures, the nucleation process that selects between outcomes is responsive to high-dimensional concentration patterns. Assembly pathways can be depicted on an energy landscape (schematic shown) as paths from a basin for unassembled components that proceed through critical nucleation seeds (barriers) to a basin for each possible final structure. Seeds that co-localize high concentration components will lower the nucleation barrier for corresponding assembly pathways. The resulting selectivity of nucleation in high-dimensional self-assembly is sufficiently expressive to perform complex pattern recognition in a manner analogous to neural computation.

The success of life on earth derives from its use of molecules to carry information and implement algorithms that control chemistry and allow organisms to respond intelligently to their environment. Genetic information encodes not only molecules with structural and chemical functionality, but also biochemical circuits such as genetic regulatory networks and signal transduction cascades that in turn process internal and external information relevant for cellular decision-making. While some biological systems may, like modern modular engineering, isolate information processing from the physical subsystems being controlled,[1] other critical decision-making may be embedded within and inseparable from processes such as metabolism, self-assembly, and structural reconfiguration. Understanding such physically-entangled computation will be necessary not only for understanding biology, but also for engineering autonomous molecular systems such as artificial cells, where it is essential to pack as much capability as possible within a limited space and with a limited energy budget.

The interplay of structure and computation is particularly rich in molecular self-assembly. In biological cells, decisions about navigation, chemotaxis, and phagocytosis are made via structural rearrangements of the cytoskeleton that integrate mechanical forces and chemical signals,[2–5] but where and how information processing occurs remains elusive. In DNA nanotechnology,[6] self-assembly of DNA tiles has been shown theoretically and experimentally to be capable of Turing-universal computation through simulation of cellular automata and Boolean circuits,[7,8] but this digital model of computation appears brittle and belabored, without a clear

analog in biology.

There is an alternative form of computation that is naturally compact and robust, and very well studied in the context of a different type of biological information processing.[9–11] Neural computation has several distinctive hallmarks: mixed analog/digital decision-making, recognition of high-dimensional patterns, reliance on the collective influence of many distributed weak interactions, robustness to noise, and an inherent ability to learn and generalize. Surprisingly, neural network models map naturally onto theoretical models of well-mixed chemical networks,[12,13] genetic regulatory networks,[14–16] and signal transduction cascades,[17,18] helping to characterize the capabilities of these systems and enabling experimental demonstrations of pattern recognition and neuromorphic computing both in cell-free biochemical circuits and within living cells.[19–21] But these well-mixed approaches still separate decision making from downstream processes.

Neural information processing principles within molecular self-assembly have been harder to discern, and perhaps at first appear as a contradiction in terms. An early thermodynamic view of how free-energy minimization in molecular self-assembly could be akin to the Hopfield model of neural associative memory did not lead to concrete realizations.[22] However, a recent kinetic view of multi-component systems that permit assembly of many distinct structures using the same components ("multifarious self-assembly")[23,24] revealed concrete connections to Hopfield associative memories[25] and models of hippocampal place cells[26] at the level of collective dynamics, even though individual molecules do not mimic individual neurons in any obvious way.

Here, we reformulate this connection as an intrinsic feature of heterogeneous nucleation kinetics and experimentally demonstrate its power for high-dimensional pattern recognition using DNA nanotechnology.[6] The phenomenon arises when the same components can form several distinct assemblies in different geometric arrangements, or shapes (Fig. 1). In this case, nucleation proceeds by spontaneous formation of a critical seed that subsequently grows to form an assembly consistent with the arrangement within the seed. Because the rate of nucleation through a given pathway depends strongly on the concentrations of the components within the seed, and there may be many distinct pathways possible, the overall rate of formation of a given shape may be a complex function of the concentration pattern. Furthermore, because components are shared between the shapes, competition for resources[27] results in a winner-take-all effect that accentuates the discrimination between concentration patterns.

## Molecular system design

To explore these principles experimentally, we take advantage of the powerful foundation provided by DNA nanotechnology for programming molecular self-assembly. The well-understood kinetics and thermodynamics of Watson-Crick base pairing[28,29] enables systematic sequence design[7] for DNA tiles that reliably self-assemble into periodic, uniquely-addressed, and algorithmically-patterned structures with 100s to 1000s of distinct tile types.[7,30–35] These classes of self-assembly differ in final structures produced and in the nature of interactions: in periodic and uniquely-addressed structures, each molecular component typically has a unique possible binding partner in each direction. For algorithmic patterns (as for multifarious assembly), at least some components have multiple possible binding partners, such that which one attaches must be decided during self-assembly.

We build on these ideas to create a molecular system capable of assembling multiple target structures (H, A, and M in Fig. 2) from a shared set of interacting components by co-localizing them in different ways. The first stage of design begins with a checkerboard arrangement in which a set S of shared tiles do not directly bind each other; then three sets of interaction mediating-tiles (also called H, A, and M) are introduced for each of the respective desired structures. This design avoids constraints from Watson-Crick complementarity, allowing almost arbitrary interactions to be engineered between S tiles. Later design stages, described below, optimized this initial layout to reduce assembly errors; Extended Data Fig. E1 describes the optimization and Extended Data Fig. E2 compares with the checkerboard design.

The basic design principles are as follows. Each interaction tile in H binds four specific S tiles together in a way that reflects neighborhood constraints between shared S tiles in structure H. These H tiles are unique to structure H and do not occur in the assembled A or M structures. Tiles in a 1:1 stoichiometric mix of S+H, S+A or S+M will have no promiscuous interactions and will assemble H, A or M respectively, as with prior work on uniquely addressable structures.[34] But a 1:1:1:1 mix of S+H+A+M, henceforth called our SHAM mix, is capable of assembling three distinct structures. This additive construction of interaction-mediating tiles is analogous to Hebbian learning of multiple memories in Hopfield neural networks.[23,25]

Extensive promiscuous interactions present in the SHAM mix could in principle lead to unplanned chimeric structures and aggregates (Extended Data Fig. E2). We combine two kinds of cooperative effects, called "proofreading" because they lead to rejection of mis-assembled tiles, to prevent such aggregates. Much like with neural networks,[36] random arrangement of tiles provides a statistical proofreading.[23] Further optimization of the tile set (Extended Data Fig. E1) confers algorithmic proofreading.[37,38] The resulting design in Fig. 2b, has 168 tiles shared across all three structures, 203 tiles shared across a pair, and 546 tiles unique to a specific shape. Our experimental implementation used 42-nucleotide single-stranded DNA tiles[34] (Fig. 2a) with sequences designed using tools from prior work[7] to reduce unintended interactions and secondary structure and ensure nearly-uniform binding energies.

To test whether proofreading was sufficient to combat promiscuity and to test the unbiased yield of different structures, we annealed all tiles at equal concentration (60 nM) in solution over 150 hours from 48 °C to 45 °C. Atomic

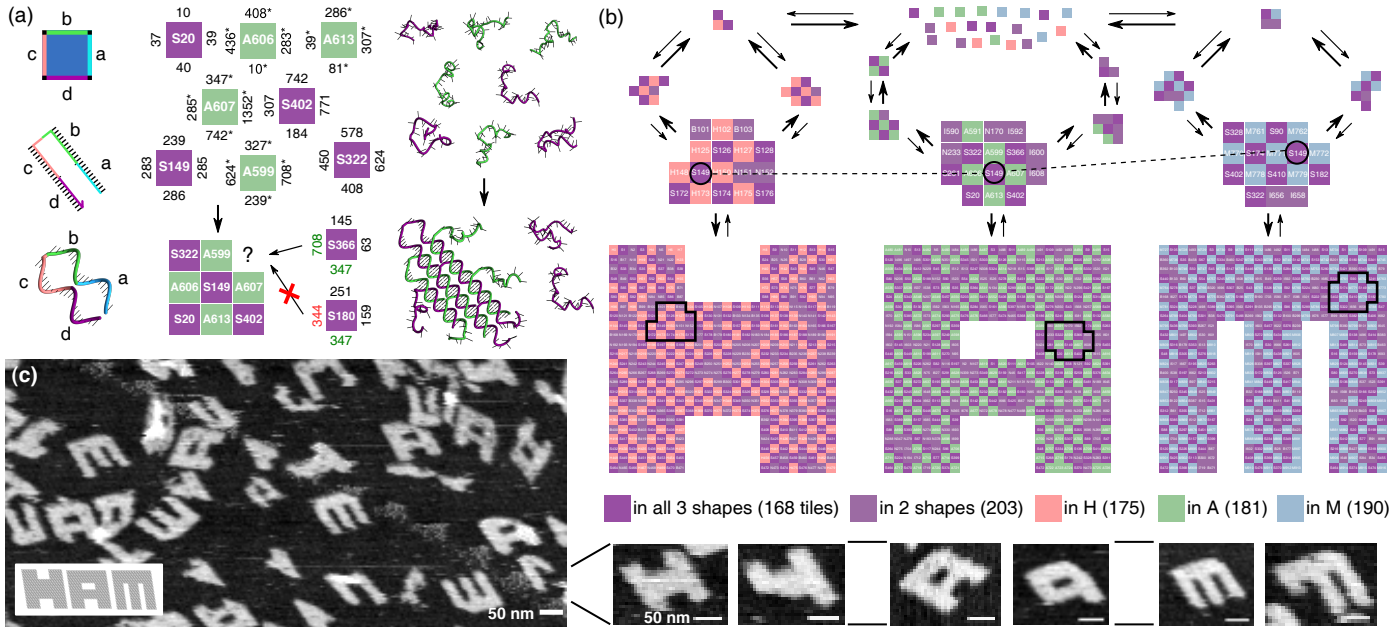


**Fig. 2 | A multifarious mixture of 917 molecular species that can assemble into three distinct structures from one set of molecules. a,** 42-nucleotide DNA strands self-assemble into 2-d structures by forming bonds with four complementary strands in solution via four 10 or 11 nucleotide domains. The strands can be abstracted as square tiles, each named and shown with distinct binding domains identified by number, such that e.g. 708 is complementary to 708*. **b,** One pool of 917 tile types assembles into three distinct shapes, H, A and M, through a multitude of pathways. While each tile occurs at most once in each shape, the shared purple species recur in multiple shapes, in distinct spatial arrangements. **c,** Annealing an equal mix of all tiles results in a mixture of fully and partially assembled H, A and M, imaged by atomic force microscope (AFM). Inset illustrates the expected slant of the shapes due to single-stranded tile geometry.

force microscopy (AFM) revealed a roughly equal yield of all three structures (Fig. 2c), despite the inequivalent thermodynamic energies of H, A, and M due to their different area-to-perimeter ratios (Fig. 3). These results indicate that yield is kinetically controlled and no one structure has intrinsically favorable kinetic pathways on the timescales probed here. Additionally, we did not observe significant chimeric structures or uncontrolled aggregation, indicating that proofreading was functioning as desired. A fraction of structures formed, however, were missing fragments at two specific corners, which could arise from asymmetric growth kinetics or lattice curvature.[33]

## Co-localization controls nucleation

To assess how kinetic pathways can be determined by nucleation and controlled by concentration patterns, we adapt classical nucleation theory[39] to consider target structures that differ in co-localization of tiles. We model the free energy of a structure $A$ with $B$ total bonds as $G(A) = \sum_{i \in A} G^i_{mc} - B\,G_{se} - \alpha$, where $\alpha$ depends on the choice of reference concentration $u_0$, $G^i_{mc} = \alpha - \log c_i/u_0$ is the chemical potential (or equivalently, translational entropy) of tile $i$ at concentration $c_i$, and $G_{se}$ is the energy of each bond in units of $RT$. $G(A)$ has competing contributions that scale with the structure's area and perimeter, and is hence maximized for certain partial assemblies called critical nucleation seeds. The formation of such seeds is often rate-limiting: once these seeds are assembled, subsequent growth is faster and mostly 'downhill' in free energy. If the nucleation rate for a given shape is dominated by a single critical nucleus $A_s$, we could use an Arrhenius-like approximation $\eta^+_{shape} \sim e^{-G(A_s)}$; in the case that multiple critical nuclei are significant, we must perform a sum (Extended Data Fig. E3).

When such analyses are applied to homogeneous crystals with uniform concentration $c_i = c$ of components, critical nuclei are simply those with the appropriate balance of size and perimeter. Heterogeneous concentration patterns require a new kind of analysis. Identifying critical seeds is now more involved since they can be arbitrarily shaped, paying in perimeter to gain high concentration tiles, and may have different sizes, with many high concentration tiles in structures resulting in smaller critical sizes. We implemented a stochastic sampling algorithm (Extended Data Fig. E3) to estimate the nucleation rate of a structure with an uneven pattern of concentrations $c_i$, with results in Fig. 3.

We can gain insight into how nucleation performs pattern recognition using the example shown in Fig. 3a, where the concentrations of some shared tiles in the SHAM mix have been enhanced. If the high concentration tiles are co-localized in structure H, such a pattern will lower kinetic barriers for the nucleation of H while maintaining high barriers for A and M since those same high concentration tiles are scattered across the structure in A and M. The typical area $K$ over which co-localization promotes nucleation depends on the temperature and the typical concentration of high tiles and can be estimated from the size of critical seeds predicted by classical nucleation theory. The nucleation rate

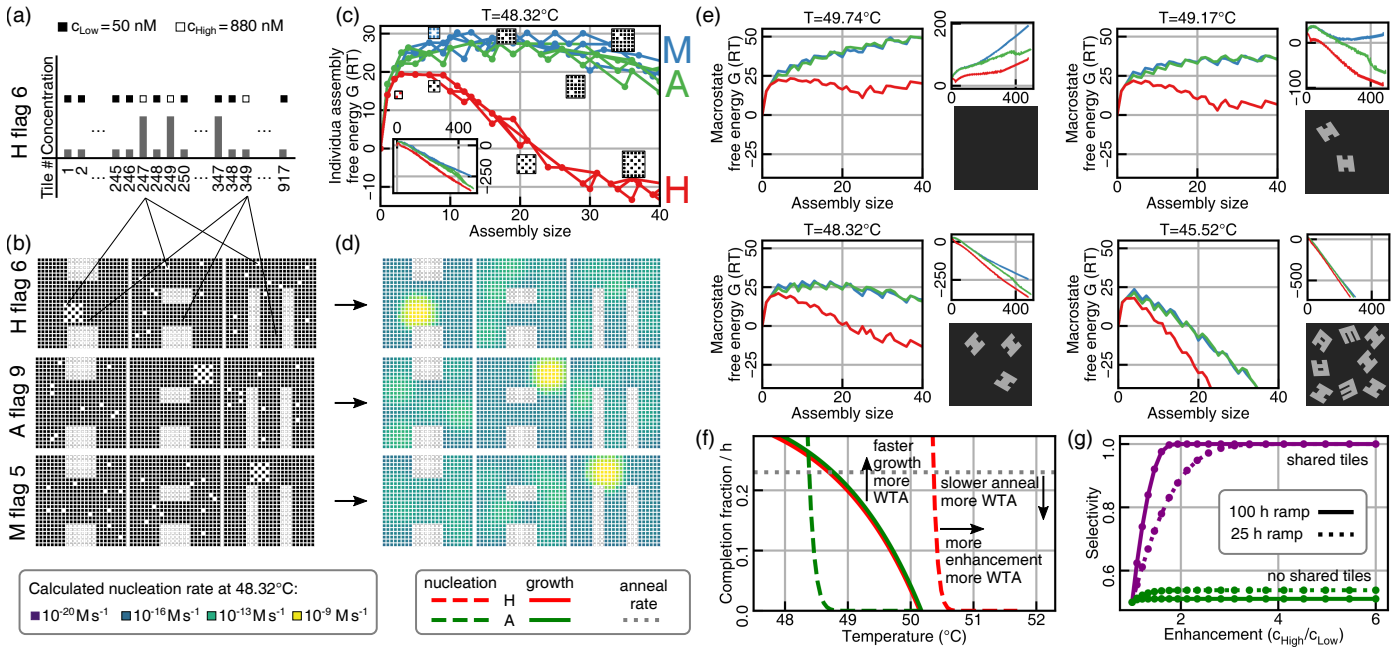


**Fig. 3 | Theory shows selective nucleation when high concentration tiles are co-localized in one shape more than in others. a, b,** A pattern enhancing the concentration of shared tiles co-localized in H but relatively dispersed in A and M. **c,** Nucleation pathways for H climb a lower nucleation barrier, with smaller critical nuclei (colored assemblies), as seen from a stochastic nucleation simulation (Supplementary Information and Data Appendix, Section 1.2). **d,** Regions predicted to participate in nucleation by the simulation for three concentration patterns (lighter colors correspond to higher participation). **e,** Assembly-size macrostate free energies and predicted AFM results at several temperatures. Varying temperature trades off selectivity for speed due to the size of the critical nucleus (and thus the scale of pattern recognition) changing differently for on-target and off-target shapes. **f,** As the dependence of nucleation and growth rates on temperature, shown here for a simple chemical reaction network model (Supplementary Information and Data Appendix, Section 1.3) favoring H, is shape-specific and changed by the tile concentration pattern, depletion of shared tiles during a temperature anneal can lead to a winner-take-all (WTA) effect. Changing growth rates, concentration patterns, and annealing rates all impact the amount of WTA. **g,** In this model, WTA leads to higher selectivity compared to systems with no shared components; for slower anneals, selectivity increases for systems with shared components, but decreases for systems with no shared components.

of a structure is high if it contains contiguous regions of area $K$ with high average (log) concentration, and is low otherwise. Since the area of critical seeds, and hence $K$, is generally larger at high temperatures, we expect a trade-off between speed and complexity of pattern recognition (Fig. 3e), with more subtle discrimination at higher temperatures (large $K$)—at the expense of slower experiments—and lower discriminatory power at lower temperatures (small $K$).

To experimentally characterize the basis of selectivity, we systematically varied the location of a $5 \times 5$ checkerboard pattern of high concentration tiles—a 'flag'—in each of the three shapes, through 37 total locations (three examples are shown in Fig. 3b). We enhanced concentrations of only shared tiles in the SHAM mix, and thus did not create additional thermodynamic bias towards any one structure. We ramped the temperature down slowly, from 48 °C to 46 °C (the expected range for nucleation, a few degrees below the melting temperatures) to provide robustness to variations in nucleation temperatures among flags in different locations. To monitor nucleation and growth in real time, we designed distinct fluorophore/quencher pairs on adjacent tiles in four locations on each shape, using tiles not shared between shapes. Each pair quenches when the local region of that specific structure assembles (Fig. 4b and Extended Data Fig. E4).

Experimental results for the three example flag concentration patterns are shown in Fig. 4c, and illustrate selective nucleation (more details in Extended Data Fig. E5). When the pattern localizes high concentration species in a structure, e.g., H, the fluorophore in the expected nucleation region of that structure quenched first and rapidly. After a delay, fluorophore signals from other parts of the same structure also dropped, indicating growth. Fluorophores on off-target structures show minimal to no quenching until very late in the experiment. AFM images from samples at the end of the experiment confirm that fluorophore quenching corresponded to selective self-assembly of complete or partial shapes. Of the 37 flag positions, roughly half exhibited robust selective nucleation and growth (Fig. 4de), while other positions were either not selective or did not grow well, for reasons we have not been able to determine.

In multifarious systems, we expect enhanced selectivity because of a competitive suppression of nucleation. If we use an annealing protocol that spends a sufficient time in a temperature range where H can nucleate and grow significantly, but A cannot nucleate (Fig. 3f), then we expect a winner-take-all (WTA) effect in which the assembly of H depletes shared tiles S and thus actively suppress nucleation of A. As shown in Fig. 4f, we see evidence for such a WTA effect in most experiments (see also Extended Data Fig. E6).

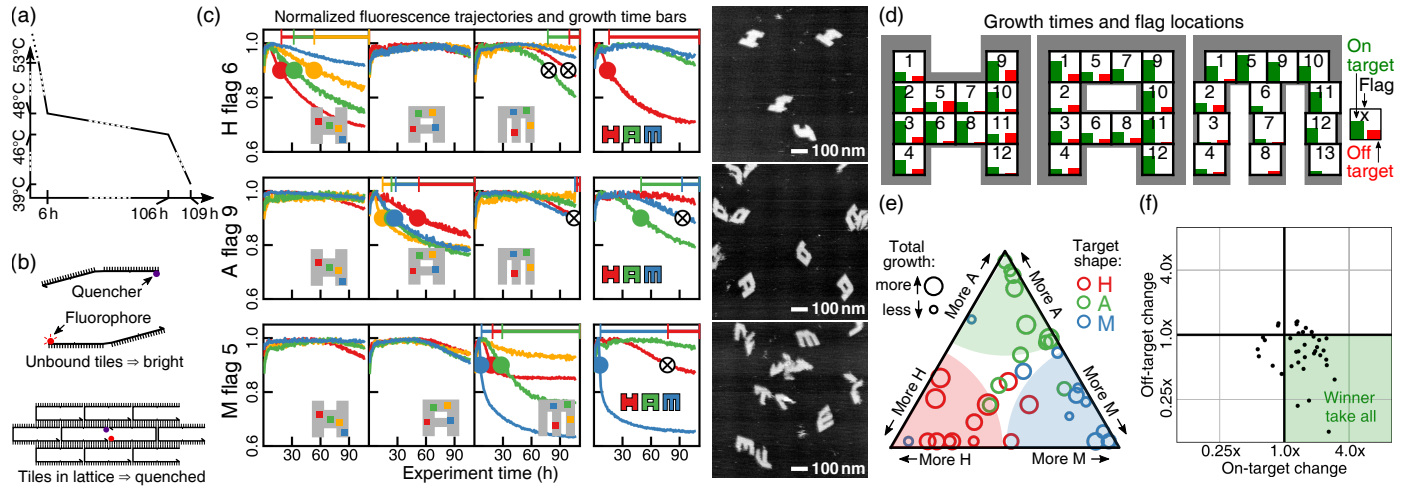


**Fig. 4 | Selective nucleation in experiments with shape-specific localized concentration patterns of shared tiles. a,** Samples were annealed with a temperature protocol that cooled from 71 °C (well above the melting temperature) to 48 °C over ∼ 6 hours, cooled to 46 °C over 100 hours, and finally was brought to 39.5 °C over 3 hours (see Extended Data Fig. E5). **b,** Fluorescence monitoring was achieved by fluorophore-quencher pairs on the 5′ ends of selected shape-specific tile strands. Fluorescence is quenched when both tiles are incorporated within a properly self-assembled local context, while smaller assemblies involving just a few strands do not effectively quench fluorescence. Four different fluorophore/quencher pairs were designed on adjacent tiles in four locations on each structure, allowing a given sample to choose one of three locations for each color, as indicated in **c**; quenching of a label indicates growth of that local region on that structure (see Extended Data Fig. E4). **c-e,** We prepared 37 different concentration patterns (three from Fig. 3 shown here) that had 12 or 13 shared tiles of increased concentration (17.6x) in checkerboard pattern in a particular $5 \times 5$ location in H, A, or M. Fluorophore quenching in multiple samples, and AFM imaging, showed that many patterns resulted in selective nucleation of the shape with the checkerboard pattern (**c**); results for each location are summarized (**d**) and plotted (**e**). **f,** Change in quenching (a measure of nucleation) of on- and off-target structures with flag patterns relative to their quenching in equimolar SHAM mixes. For most flags, the absolute nucleation rate of off-target shapes is reduced upon increasing concentrations of shared tiles, supporting a winner-take-all effect (see Extended Data Fig. E6).

Such a winner-take-all effect can enhance the effect of small differences in nucleation kinetics.

## Pattern recognition by nucleation

Our work thus far shows that the space of all concentration patterns $\mathbf{C} = \mathcal{R}^n$ can be composed of regions that result in the selective assembly of each of H, A and M respectively at a specific temperature; see Fig. 5a. In fact, these regions together represent the phase diagram of this self-assembling system.[40] Phase boundaries can be seen as decision boundaries where selectivity is low. Phase boundaries of traditionally studied physical systems are usually low dimensional and not fruitfully interpreted as decision boundaries. However, in multi-component heterogeneous systems like ours, the phase diagram is naturally high dimensional since the concentrations of all 917 components must be specified. Further, phase boundaries in disordered many-body systems tend to be complex and thus implicitly solve complex pattern recognition problems, a perspective that also underlies Hopfield's Associative Memory in neural networks.[25,41]

In this way, selective nucleation can be seen as solving a particular pattern recognition problem based on which molecules are co-localized in the designed structures. Similar co-localization-based decision boundaries arise in the context of neural place cells studied by the Mosers[24,42–44] and have been shown to be complex enough to solve pattern recognition problems and permit statistically robust learning.

Having demonstrated that multifarious self-assembly can solve a specific pattern recognition problem based on co-localization, could different molecules be designed to solve other arbitrarily-given pattern recognition problems, e.g. that shown in Fig. 5a? Here, the grayscale value of each pixel position in the $30 \times 30$ images is taken to represent the concentration of a distinct molecule. Instead of synthesizing new molecules with new interactions to solve the above challenge, we equivalently show that the design problem is solvable with our existing molecules by an optimized choice of a pixel-to-tile map $\theta$, that is by choosing which of our existing tiles should correspond to which pixel position (Fig. 5b). In addition to saving DNA synthesis costs, this approach also helps demonstrate that a random molecular design can be exploited, *ex post facto*, to solve a specific computational problem by modifying how the problem is mapping onto physical components, as done in reservoir computing.[45]

We specified our design problem by picking arbitrary images as training sets shown in Fig. 5d. Note that images in one class share no more resemblance than images across classes, e.g., class H is Hodgkin, Hopfield, Horse etc, though the number of pixels and grayscale histogram were standardized across images (see Methods). In this way, the number of distinct images per class (6 in the experiments presented below) tests the flexibility of decision surfaces inherent to this self-assembling molecular system as a classifier.

We then used an optimization algorithm (see Fig. 5c and Methods) on $\theta$ that sought to maximize nucleation of the on-target structure for the concentration pattern corresponding to each image while also minimizing off-target nucleation.

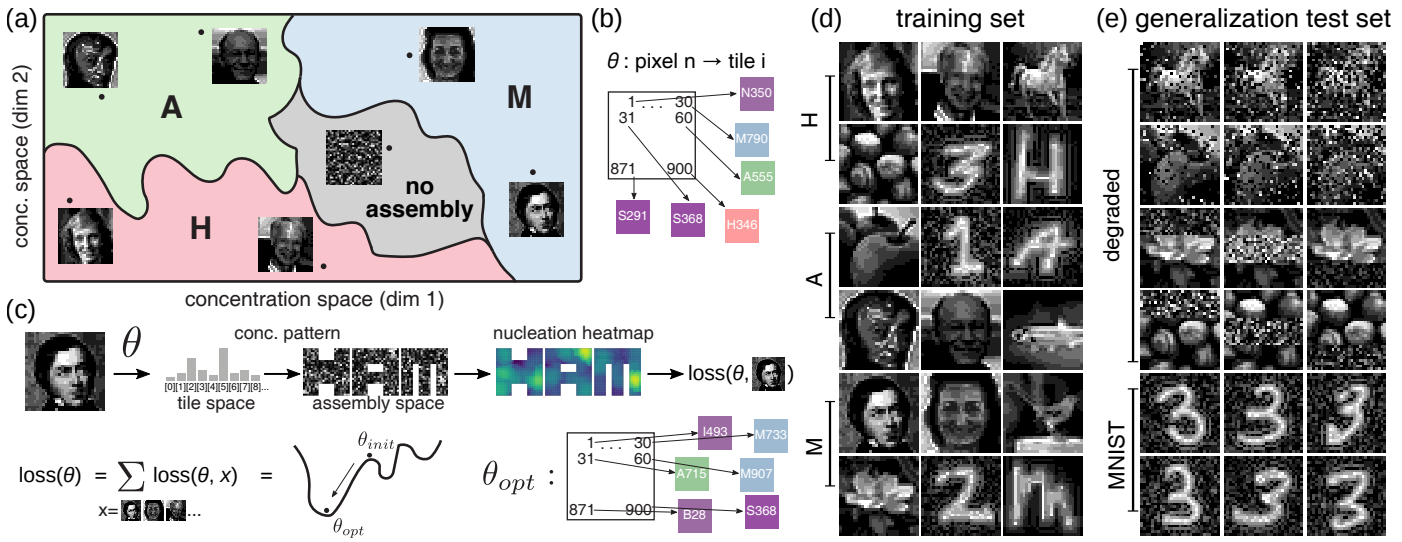


**Fig. 5 | Design of self-assembly phase diagrams to solve pattern recognition problems. a,** Phase diagram shows desired outcomes of kinetically controlled self-assembly in different regions of $N = 917$ dimensional concentration space (2d schematic shown). Each grayscale image represents a vector of tile concentrations. **b,** $\theta$ specifies which pixel location corresponds to which tile. **c,** Given a map $\theta$, any image can be converted to a tile concentration vector by associating the grayscale value of pixel location $n$ with the concentration of the corresponding tile $i = \theta(n)$. We compute the 'loss' for a given pixel-to-tile map $\theta$ using simulations to estimate the nucleation rates of desired and undesired structures for each image and summing over a training set. Stochastic optimization in $\theta$ space gives a putative optimal $\theta_{opt}$ that we used for experiments. **d,** Images used for training. **e,** Additional images used to test generalization power.

That is, our algorithm sought to map high concentration pixels in each image (e.g., Moser) to co-localized tiles in the corresponding on-target structure (here, M) to enhance nucleation, while mapping those same pixels to scattered tiles in undesired structures (here, A and H). Note that this map $\theta$ is simultaneously optimized for all images and not independently for each image. Hence no map $\theta$ might be able to perfectly satisfy all the above requirements simultaneously for all images in all classes; analogous to associative memory capacity,[23,25,41] we explore the limits of this classifier in Extended Data Fig. E7.

In experiments, we then enhanced concentrations of tiles in the SHAM mix in accordance to each of the 18 training images (using the optimized $\theta$) and annealed each of the 18 mixes with a 150 h ramp from 48 °C to 45 °C. We found that the 18 training images yielded highly selective correct nucleation, as verified by AFM imaging and real-time fluorescence quenching (Fig. 6 and Extended Data Fig. E8).

We also tested 12 degraded images and 6 alternate handwriting images (Fig. 5e). We find successful pattern recognition for random speckle distortions, and all but one partly obscured image. The ability to recognize distorted images, not present in a training set, is a critical aspect of learning in neural networks since it tests the ability to generalize. A given neural network architecture can be naturally robust to certain families of distortions (e.g., convolutional networks can handle translation) but not others (e.g., dilation). Furthermore, since nucleation is a cooperative process, often dominated by one or a few critical seeds involving just a handful of tiles, flipping of random uncorrelated pixels and obscuring parts of an image that do not involve those critical pixel combinations will not inhibit nucleation – demonstrating robustness. On the other hand, only 3 of the 6 alternate handwritten digits were correctly recognized by self-assembly, indicating a lack of robustness to this type of variation, with our training protocol.

## Discussion

The phenomenon of pattern recognition by multifarious self-assembly that we demonstrated may be exploited by complex evolved or designed systems. For example, the phase boundaries for multi-component condensates governing genetic regulation[46] may also contain similar inherent information-processing capabilities. In such a case, the 'pixel-to-tile' map would instead correspond to a layer of phosphorylation or binding circuitry that activates or deactivates specific self-assembling components based on the levels of upstream information-bearing molecular signals. Within future artificial cell-like molecular robots, nucleation may be an especially compact way to implement decision-making within the limited space constraints.

To better understand the information-processing potential of nucleation, we may treat this physical process as a machine learning model. A key issue is how the complexity of decision surfaces, quantified, e.g., by the VC dimension,[9] depends on underlying physical aspects of self-assembly such as concentration, temperature, annealing speed, non-equilibrium effects such as winner-take-all, number of molecular species, binding free energies and their specificity, and the geometry of structures. Our work already suggests that temperature mediates a trade-off between speed, accuracy, and complexity of pattern recognition; at higher temperatures, nucleation seeds are larger, allowing discrimination based on higher order correlations

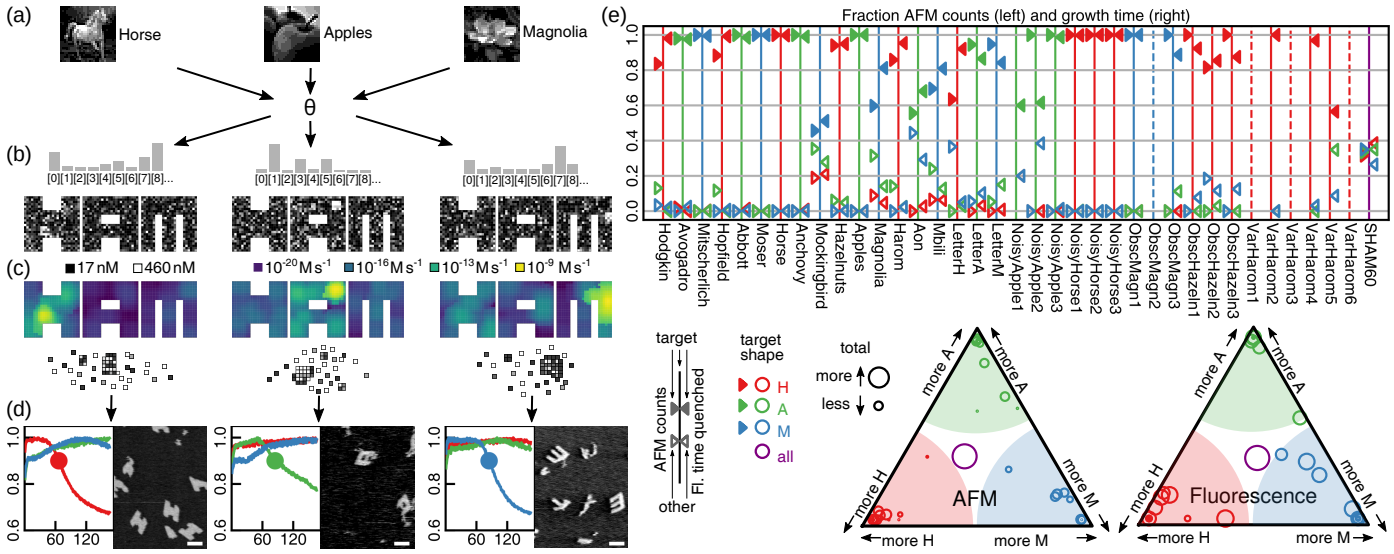


**Fig. 6 | Pattern recognition results with a pre-existing multifarious system. a–c,** All images (three shown) are converted (**a**) through a single pixel-to-tile map $\theta$ to vectors of tile concentrations (**b**), which are shown mapped onto tile locations in each shape, with nucleation rate predictions from the Stochastic Greedy Model (**c**). **d,** Normalized fluorescence over time in hours (one label per shape; other label configurations shown in Extended Data Fig. E8) during a 150 hour temperature ramp from 48 °C to 45 °C, and final AFM images (with 100 nm scale bars). **e,** Summary of results for both fluorescence and AFM for all 36 images, and a uniform 60 nM tile concentration control sample. Above, colors of vertical lines indicate the target shape for the each pattern, while triangular markings of each color indicate the relative fraction of growth time (on right) or fraction of shapes counted in AFM images (on left) for the corresponding shape (solid markings indicate target shape). Dashed lines indicate samples with no significant quenching or observed shapes. Below, ternary plots summarize the same results, with proximity to triangle corners indicating relative fractions of growth time (right) or counted shapes (left), and circle size indicating overall growth time (right) or total number of shapes (left).

in the concentration patterns, but the physical process is also correspondingly slower. Indeed, unlike many prior relationships between physics and computation, computation here exploits the inevitable inherently stochastic nature of nucleation. Monomers must make many unsuccessful attempts at forming a critical seed for both on- and off-target structures, with repeated disassembly before discovering the seed for the correct pattern recognition outcome, much like the backtracking inherent to stochastic search algorithms.[47] In well-mixed chemical systems, a formal connection between stochastic chemical kinetics and computational solutions to NP-complete Boolean satisfiability problems has been established,[48] suggesting a possible approach for characterizing the power of stochastic nucleation.

Viewing nucleation as a machine learning model raises the question of whether there is a natural physical implementation of learning. In this work, learning was implemented in a manner reminiscent of reservoir computing:[45,49] molecules with a fixed set of interactions could nevertheless solve an arbitrary problem by simply training, on a computer, for how the problem is mapped to components of the fixed existing system. However, the similarity of the framework here to neural models of associative memory,[25] especially those based on random co-localization,[24,42,43] allow the interactions to potentially be learned in a Hebbian manner by a natural physical process. For example, a fourth or fifth structure can be added by adding new unique tiles that mediate interactions needed for such structures. Further, if these interaction-mediating tiles could be physically created or activated in response to environmental inputs, e.g., through proximity-based ligation, molecular systems could autonomously learn new self-assembling behaviors from examples[50–52] without the need for computer-based learning.

The connection between self-assembly and neural network computation raises a great many questions that will be productive for further exploration, but perhaps the broadest one is a variant on Anderson's observation that 'more is different'.[53] Anderson was referring to the fact that when systems of a great many copies of the same simple component are considered, as in statistical mechanics or fluid dynamics to take canonical examples, phenomena that are best understood at a higher level may emerge. Biology seems to (also) explore a different sense of 'more is different': in many cases, it makes use of just a few copies of a great many different types of components.[1] Here too there may be phenomena that naturally emerge in the 'large $N$ limit': robustness, programmability, and information-processing. Such things are best explored in information-rich model systems devoid of the distracting complexities of biology, and this is what is provided by DNA nanotechnology. Indeed, there is already evidence for 'more is different' phenomena that can occur when scaling up the number of components: whereas self-assembled few-component DNA structures are often sensitive to sequence details and molecular purity, thus taking years to refine experimentally, DNA origami[54] uses hundreds of components and usually works on the first try, even with unpurified strands, imprecise stoichiometry, and no sequence optimization. Similarly, uniquely-addressed multi-component single-stranded tile systems[34,55,56] have robustly scaled up to thousands of components due to the richness

of the molecular information. Our work adds sophisticated information-processing as a new emergent phenomenon for self-assembly which gains highly programmable and potentially learnable phase boundaries to solve specific pattern recognition problems in the multicomponent limit, as found earlier in large $N$ neural networks.[41] Consequently, this neural network inspired perspective may help recognize and guide understanding of high-dimensional molecular systems where information-processing is deeply entangled within physical processes, whether in biology or in molecular engineering: multicomponent liquid condensates, multicomponent active matter, and other systems might have similar programmable and learnable phase boundaries.

## References


1. Hartwell, L. H., Hopfield, J. J., Leibler, S. & Murray, A. W. "From molecular to modular cell biology". *Nature* **402,** C47–C52 (1999) (cit. on pp. 1, 7).
2. Fletcher, D. A. & Mullins, R. D. "Cell mechanics and the cytoskeleton". *Nature* **463,** 485–492 (2010) (cit. on p. 1).
3. Holy, T. E. & Leibler, S. "Dynamic instability of microtubules as an efficient way to search in space". *Proceedings of the National Academy of Sciences* **91,** 5682–5685 (1994) (cit. on p. 1).
4. Lee, C.-Y. *et al.* "*Coccidioides* endospores and spherules draw strong chemotactic, adhesive, and phagocytic responses by individual human neutrophils". *PLoS ONE* **10,** e0129522 (2015) (cit. on p. 1).
5. Floyd, C., Levine, H., Jarzynski, C. & Papoian, G. A. "Understanding cytoskeletal avalanches using mechanical stability analysis". *Proceedings of the National Academy of Sciences* **118** (2021) (cit. on p. 1).
6. Seeman, N. C. & Sleiman, H. F. "DNA nanotechnology". *Nature Reviews Materials* **3,** 17068 (2018) (cit. on pp. 1, 2).
7. Woods, D. *et al.* "Diverse and robust molecular algorithms using reprogrammable DNA self-assembly". *Nature* **567,** 366 (2019) (cit. on pp. 1, 2, 10, 11).
8. Rothemund, P. W. K. & Winfree, E. "The program-size complexity of self-assembled squares". *Proceedings of the Thirty-Second Annual ACM Symposium on Theory of Computing,* 459–468 (2000) (cit. on p. 1).
9. Hertz, J., Krogh, A. & Palmer, R. G. *Introduction to the Theory of Neural Computation* (CRC Press, 1991) (cit. on pp. 2, 6).
10. Dayan, P. & Abbott, L. F. *Theoretical Neuroscience: Computational and Mathematical Modeling of Neural Systems* (MIT press, 2005) (cit. on p. 2).
11. Goodfellow, I., Bengio, Y. & Courville, A. *Deep Learning* (MIT press, 2016) (cit. on p. 2).
12. Rössler, O. E. "A synthetic approach to exotic kinetics (with examples)". *Physics and Mathematics of the Nervous System,* 546–582 (1974) (cit. on p. 2).
13. Hjelmfelt, A., Weinberger, E. & Ross, J. "Chemical implementation of neural networks and Turing machines". *Proceedings of the National Academy of Sciences* **88,** 10983–10987 (1991) (cit. on p. 2).
14. Buchler, N. E., Gerland, U. & Hwa, T. "On schemes of combinatorial transcription logic". *Proceedings of the National Academy of Sciences* **100,** 5136–5141 (2003) (cit. on p. 2).
15. Mjolsness, E., Sharp, D. H. & Reinitz, J. "A connectionist model of development". *Journal of Theoretical Biology* **152,** 429–453 (1991) (cit. on p. 2).
16. Lewis, J. E. & Glass, L. "Steady states, limit cycles, and chaos in models of complex biological networks". *International Journal of Bifurcation and Chaos* **1,** 477–483 (1991) (cit. on p. 2).
17. Bray, D. "Protein molecules as computational elements in living cells". *Nature* **376,** 307–312 (1995) (cit. on p. 2).
18. Helikar, T., Konvalina, J., Heidel, J. & Rogers, J. A. "Emergent decision-making in biological signal transduction networks". *Proceedings of the National Academy of Sciences* **105,** 1913–1918 (2008) (cit. on p. 2).
19. Qian, L., Winfree, E. & Bruck, J. "Neural network computation with DNA strand displacement cascades". *Nature* **475,** 368–372 (2011) (cit. on p. 2).
20. Cherry, K. M. & Qian, L. "Scaling up molecular pattern recognition with DNA-based winner-take-all neural networks". *Nature* **559,** 370–376 (2018) (cit. on p. 2).
21. Rizik, L., Danial, L., Habib, M., Weiss, R. & Daniel, R. "Synthetic neuromorphic computing in living cells". *In Review (Nature portfolio, Research Square)* (2021) (cit. on p. 2).
22. Conrad, M. *Self-assembly as a mechanism of molecular computing*. in *Images of the Twenty-First Century. Proceedings of the Annual International Engineering in Medicine and Biology Society* (IEEE, Seattle, WA, USA, 1989), 1354–1355 (cit. on p. 2).
23. Murugan, A., Zeravcic, Z., Brenner, M. P. & Leibler, S. "Multifarious assembly mixtures: Systems allowing retrieval of diverse stored structures". *Proceedings of the National Academy of Sciences* **112,** 54–59 (2015) (cit. on pp. 2, 6, 10).
24. Zhong, W., Schwab, D. J. & Murugan, A. "Associative pattern recognition through macro-molecular self-assembly". *Journal of Statistical Physics* **167,** 806–826 (2017) (cit. on pp. 2, 5, 7, 12).
25. Hopfield, J. J. "Neural networks and physical systems with emergent collective computational abilities". *Proceedings of the National Academy of Sciences* **79,** 2554–2558 (1982) (cit. on pp. 2, 5–7).
26. Moser, E. I., Kropff, E. & Moser, M.-B. "Place cells, grid cells, and the brain's spatial representation system". *Annual Review of Neuroscience* **31,** 69–89 (2008) (cit. on p. 2).
27. Genot, A. J., Fujii, T. & Rondelez, Y. "Computing with competition in biochemical networks". *Physical Review Letters* **109,** 208102 (2012) (cit. on p. 2).
28. SantaLucia, J. & Hicks, D. "The thermodynamics of DNA structural motifs". *Annual Review of Biophysics and Biomolecular Structure* **33,** 415–440 (2004) (cit. on p. 2).
29. Sengar, A., Ouldridge, T. E., Henrich, O., Rovigatti, L. & Šulc, P. "A primer on the oxDNA model of DNA: When to use it, how to simulate it and how to interpret the results". *Frontiers in Molecular Biosciences* **8** (2021) (cit. on p. 2).

30. Winfree, E., Liu, F., Wenzler, L. A. & Seeman, N. C. "Design and self-assembly of two-dimensional DNA crystals". *Nature* **394,** 539–544 (1998) (cit. on p. 2).
31. Rothemund, P. W. K. *et al.* "Design and characterization of programmable DNA nanotubes". *Journal of the American Chemical Society* **126,** 16344–16352 (2004) (cit. on p. 2).
32. Wang, W. *et al.* "Self-assembly of fully addressable DNA nanostructures from double crossover tiles". *Nucleic Acids Research* **44,** 7989–7996 (2016) (cit. on p. 2).
33. Yin, P. *et al.* "Programming DNA tube circumferences". *Science* **321,** 824–826 (2008) (cit. on pp. 2, 3, 14).
34. Wei, B., Dai, M. & Yin, P. "Complex shapes self-assembled from single-stranded DNA tiles". *Nature* **485,** 623–626 (2012) (cit. on pp. 2, 7, 10).
35. Ke, Y. *et al.* "DNA brick crystals with prescribed depths". *Nature Chemistry* **6,** 994–1002 (2014) (cit. on p. 2).
36. Hopfield, J. J. "Neurodynamics of mental exploration". *Proceedings of the National Academy of Sciences* **107,** 1648–1653 (2010) (cit. on p. 2).
37. Winfree, E. & Bekbolatov, R. *Proofreading tile sets: Error correction for algorithmic self-assembly*. in *DNA Computing (Lecture Notes in Computer Science)* (eds Chen, J. & Reif, J.) **2943** (Springer Berlin Heidelberg, 2004), 126–144 (cit. on pp. 2, 14).
38. Evans, C. G. & Winfree, E. *Optimizing tile set size while preserving proofreading with a DNA self-assembly compiler*. in *DNA Computing and Molecular Programming (Lecture Notes in Computer Science)* (eds Doty, D. & Dietz, H.) **11145** (Springer International Publishing, 2018), 37–54 (cit. on pp. 2, 10, 14).
39. Frenkel, D. & Smit, B. *Understanding Molecular Simulation: From Algorithms to Applications* (Academic Press, 2002) (cit. on pp. 3, 10).
40. Murugan, A., Zou, J. & Brenner, M. P. "Undesired usage and the robust self-assembly of heterogeneous structures". *Nature Communications* **6,** 6203 (2015) (cit. on p. 5).
41. Amit, D., Gutfreund, H. & Sompolinsky, H. "Storing infinite numbers of patterns in a spin-glass model of neural networks". *Physical Review Letters* **55,** 1530–1533 (1985) (cit. on pp. 5, 6, 8).
42. Moser, E. I., Moser, M.-B. & McNaughton, B. L. "Spatial representation in the hippocampal formation: a history". en. *Nature Neuroscience* **20,** 1448–1464 (2017) (cit. on pp. 5, 7).
43. Battaglia, F. P. & Treves, A. "Attractor neural networks storing multiple space representations: A model for hippocampal place fields". *Physical Review E* **58,** 7738–7753 (1998) (cit. on pp. 5, 7).
44. Monasson, R. & Rosay, S. "Transitions between spatial attractors in place-cell models". *Physical Review Letters* **115,** 098101 (2015) (cit. on p. 5).
45. Tanaka, G. *et al.* "Recent advances in physical reservoir computing: A review". *Neural Networks* **115,** 100–123 (2019) (cit. on pp. 5, 7).
46. Hnisz, D., Shrinivas, K., Young, R. A., Chakraborty, A. K. & Sharp, P. A. "A phase separation model for transcriptional control". *Cell* **169,** 13–23 (2017) (cit. on p. 6).
47. Hoos, H. H. & Stützle, T. *Stochastic Local Search: Foundations and Applications* (Elsevier, 2004) (cit. on p. 7).
48. Winfree, E. *Chemical reaction networks and stochastic local search*. in *DNA Computing and Molecular Programming (Lecture Notes in Computer Science)* **11648** (2019), 1–20 (cit. on p. 7).
49. Wright, L. G. *et al.* "Deep physical neural networks trained with backpropagation". *Nature* **601,** 549–555 (7894 2022) (cit. on p. 7).
50. Baum, E. "Building an associative memory vastly larger than the brain". *Science* **268,** 583–585 (1995) (cit. on p. 7).
51. Mills, A. P., Yurke, B. & Platzman, P. M. "Article for analog vector algebra computation". *Biosystems* **52,** 175–180 (1999) (cit. on p. 7).
52. Lakin, M. R. & Stefanovic, D. "Supervised learning in adaptive DNA strand displacement networks". *ACS Synthetic Biology* **5,** 885–897 (2016) (cit. on p. 7).
53. Anderson, P. W. "More is different: broken symmetry and the nature of the hierarchical structure of science." *Science* **177,** 393–396 (1972) (cit. on p. 7).
54. Rothemund, P. W. K. "Folding DNA to create nanoscale shapes and patterns". *Nature* **440,** 297–302 (2006) (cit. on p. 7).
55. Ke, Y., Ong, L. L., Shih, W. M. & Yin, P. "Three-dimensional structures self-assembled from DNA bricks". *Science* **338,** 1177–1183 (2012) (cit. on p. 7).
56. Ong, L. L. *et al.* "Programmable self-assembly of three-dimensional nanostructures from 10,000 unique components". *Nature* **552,** 72–77 (2017) (cit. on p. 7).

## Methods

**Multifarious DNA tile system design.** Prior theoretical proposals[23,57] for multifarious mixtures require each component to accept multiple strongly binding partners at each binding site. However, in DNA tile assembly, each binding site can usually only bind its Watson-Crick complement, and not an arbitrary set of other domains. Hence, we used an alternate approach: we assumed three structures made of entirely unique tiles and ran a merging algorithm that attempted to reuse tiles in a roughly checkerboard pattern across structures. The algorithm accepted merges if consequences for unintentional binding between other tiles were minimal. After determining the abstracted shared and tile layout in this way, we designed DNA sequences reflecting this layout.

The three target shapes were drawn on a 24 $\times$ 24 single-stranded tile (SST) molecular canvas,[34] at an abstract level, with each location in each shape initially a being unique tile with four abstract binding sites referred to as 'glues'. (After sequence design, matching glues will correspond to binding pairs of complementary sequence domains.) Edges of the shapes used a special 'null glue' that is intended to have no valid binding partner. In total, this initial design had 2,706 glues, and 1,456 tiles. The three shapes were then processed through a 'merging' algorithm that attempted to reuse the same tiles in different shapes. Randomly choosing two tiles in two different shapes (with null glues on the same sides of each tile, if any), each step of the algorithm attempted to make the two tiles identical by reusing the same four glues in both, and propagating the changes in the glues to all places they occurred within all shapes, starting with the neighboring tiles (e.g., Extended Data Fig. E1a). To avoid having these changes create undesired growth pathways, for example, allowing chimera of multiple shapes, the modified set was checked after each trial merging step for two criteria from algorithmic self-assembly (Extended Data Fig. E1b). The self-healing criterion requires that, for any correct subassembly of any shape, while attachments of the wrong tile for a particular location may take place by one bond, only the correct tile can attach by two or more bonds.[58] The second-order sensitivity criterion requires that, for any correct subassembly of any shape, if an incorrect attachment by one bond takes place, the incorrectly attached tile will not create a neighborhood where an additional incorrect tile can attach by two bonds, and thus the initial error will be likely to fall off.[38] These two criteria, which are trivially satisfied when every tile and bond is unique to a particular location, continue to be satisfied after each merging step. Thus, we ensure that there is at least a minimum barrier to continued incorrect growth in a regime where tile attachment by two or more bonds is favorable, and attachment by one bond is unfavorable, which is the case close to the melting temperature of most DNA tile assembly systems.[59,60]

The algorithm repeatedly merged tiles that satisfied the two criteria until no further acceptable merges were possible. As each merge could affect the acceptability of later merges by changing the glues around each tile, in order to guide the algorithm toward a sequence of merges more likely to be compatible, the algorithm was initially restricted to considering an alternating 'checkerboard' subset of tiles, which, apart from edges, were likely to be merge-able. After exhausting possible merges of these subsets, the algorithm then attempted merges using all tiles in the system. After repeating this stochastic algorithm multiple times, and selecting the system with the smallest number of tiles, the final resulting system had 698 binding domains and 917 tiles, with 371 of tiles shared between at least two shapes (Extended Data Fig. E1c).

After the assignment of abstract binding domains to each tile by the merging algorithm, the sequences for the binding domains, and thus tiles themselves, were generated using the sequence design software of Woods and Doty et al.[7] Tiles used a standard SST motif, with alternating 10 and 11 nt binding domains, designed to have similar binding strengths. Following Woods and Doty et al,[7] we set a target range of -8.9 to -9.2 kcal/mol for a single domain at 53 °C, which was between the melting temperature and growth temperature for their system. Null binding domains on the edges of shapes, not intended to bind to any other tiles, were assigned poly-T sequences.

**Models of nucleation.** To model the dependence of the nucleation rates of the three shapes on patterns of unequal concentration, we developed a simple nucleation model based on the stochastic generation of possible nucleation pathways and critical nuclei. The model estimates nucleation rates by analyzing stochastic paths generated in a greedy manner by making single-tile additions starting from a particular monomer in the system. At each step, all favorable attachments are added and then an unfavorable attachment is performed with probability weighted by the relative free-energy differences of the available tile attachment positions. When multiple favorable attachments are available, the most favorable attachment is made deterministically. This procedure is repeated for many paths over all possible initial positions within the shape considered, and the barrier (highest free energy state visited in 'growing' a full structure) is recorded for each path. A nucleation rate is estimated by assuming an equilibrium occupation of this barrier state (Arrenhius' approximation[39]) and summing over the kinetics of the available attachments from this state. See Extended Data Fig. E3 and Supplementary Information and Data Appendix, Section 1.2 for a detailed discussion. The approximations here could be improved by running fully reversible simulations, e.g., using Forward Flux Sampling.[61]

**Fluorophore labels, DNA synthesis, and growth.** Sites for fluorophore and quencher modifications were chosen

to avoid edges, modify only unshared tiles, and provide a reasonable distribution of locations on each shape. Fluorophores were chosen for spectral compatibility and temperature stability.[62] ROX, ATTO550, and ATTO647N were paired with Iowa Black RQ, and FAM was paired with Iowa Black FQ. Both fluorophore and quencher modifications were made on the 5' ends of tiles; to sufficiently co-localize fluorophores and quenchers, one tile in the label pair used a reversed orientation (Fig. 4a). Fluorophore labels are discussed in detail in Supplementary Information and Data Appendix, Section 2.

Tiles without fluorophore or quencher modifications were ordered unpurified (desalted) and normalized to 400 µM in TE buffer (Integrated DNA Technologies). Strands with fluorophore or quencher modifications were ordered HPLC-purified and normalized to 100 µM. Individual tiles were mixed, in the concentration patterns used for experiments, using an Echo 525 acoustic liquid handler (Beckman Coulter). Samples used TEMg buffer (TE buffer with 12.5 mM $MgCl_2$) in a total volume of $\sim$ 20 µL. Flag experiments used a 50 nM base concentration of unenhanced tiles, and an 880 nM concentration of enhanced concentration tiles, while pattern recognition experiments employed tiles with nominal concentrations between 16.67 nM to 450 nM, which were then quantized into ten discrete values to simplify mixing and conserve material (see Supplementary Information and Data Appendix, Section 1.7). Fluorophore and quencher-modified tile locations always had tiles mixed at the lowest concentration used in the experiment. Given that unpurified synthetic oligonucleotides typically have less than 40% to 60% of the molecules being full length, it is remarkable (though consistent with Woods and Doty et al[7]) that this did not prevent successful pattern recognition by nucleation.

For flag experiments, and pattern recognition of trained images, four samples were prepared per concentration pattern: one sample for each shape with all four fluorophore labels on only that shape, to monitor growth of multiple regions on each shape, and an additional sample with one fluorophore on each shape: ROX, ATTO550 ('five'), and ATTO647N ('six') on H, A, and M respectively. For pattern recognition of test images, for experiment size reasons, only the lattermost sample was prepared.

After transferring 20 µL to PCR tubes, samples were grown in an mx3005p quantitative PCR (qPCR) machine (Agilent), in order to provide a program of controlled temperature over time while monitoring fluorescence. Growth protocols began with a ramp from 71 °C to 53 °C over 40 minutes to ensure any potentially preexisting complexes were melted, and then a slower ramp from 53 °C to an initial growth temperature at 1 °C per hour. At this point, three different protocols were used. For constant temperature flag growth experiments, the growth temperature was 47 °C, and this was held for 51 hours. For temperature ramp flag growth, the initial growth temperature was 48 °C, which was reduced over 100 hours to 46 °C. For pattern recognition, a ramp from 48 °C to 45 °C over 150 hours was used. For constant temperature experiments, fluorescence readings were taken every 12 minutes, and for other experiments, every 30 minutes. After the growth period, temperature was lowered to 39 °C at 1 °C per 26 minutes. See Supplementary Information and Data Appendix, Sections 4 and 5 for temperature protocols plotted as a function of time. Because of the small sample size and long experiment duration, great care to avoid evaporation was necessary. Once protocols were finished, samples were stored at room temperature until ready for AFM imaging.

AFM imaging was performed using a FastScan AFM (Bruker) in fluid tapping mode. To achieve better images, two techniques were combined: sample warming to prevent nonspecific clumping of structures, and washing with Na-supplemented buffer to prevent smaller material, such as unbound, single DNA tile strands, from adhering to the mica surface. Each sample was diluted 50x into TEMg buffer with an added 100 mM NaCl, then warmed to approximately 40 °C for 15 minutes. 50 µL of the sample mix was deposited on freshly-cleaved mica, then left for two minutes. As much liquid as possible was pipetted off of the mica and discarded, then immediately replaced with Na-supplemented buffer again, and mixed by pipetting up and down. This washing process of buffer removal and addition was repeated twice with added-Na buffer, then once with TEMg buffer to remove remaining Na, before imaging was performed in TEMg buffer. As adhesion of DNA to mica is dependent upon the ratio of monovalent and divalent cations in the imaging buffer, this process was meant to ensure that unbound tiles were removed during the washing process where Na and Mg were present, while imaging itself took place with only Mg, so that the lattice structures would be more strongly adhered to the surface, resulting in better image quality.

**Fluorescence and AFM data analysis.** Fluorophore signals are known to be affected by extraneous factors such as temperature, pH, secondary structure, and the local base sequence near the fluorophore,[62] which complicates quantitative interpretation of absolute fluorescence levels. Our own control experiments also illustrated effects due to partial assembly intermediates as well as due to the total amount of single stranded DNA in solution (Supplementary Information and Data Appendix, Section 2). For this reason, the fluorescence of each fluorophore was normalized to the maximum raw fluorescence value of that fluorophore in that particular sample, and the *time* at which the fluorescence signal decreased by 10% was then used as a measure of the extent of nucleation that appears less sensitive to these artifacts (Extended Data Fig. E4). The duration between the point of 10% quenching and the end of the growth segment of the experiment was defined as the 'growth time' for that fluorophore label; the growth time was defined as 0 in the

event of quenching never reaching 10%. For concentration patterns with four samples with different fluorophore arrangements, the total growth time of a shape was defined as the average of the growth time of the five total fluorophore labels on the shape across the four samples (four in the shape-specific sample, and one in the each-shape sample), while for concentration patterns with only one sample, the growth time of the corresponding fluorophore label was used. As the position of the fluorophore within the shape, relative to where nucleation occurs, has a substantial influence on growth time measurements, the considerable variability in these measurements relative to the true nucleation kinetics must be acknowledged.

For flag experiments, AFM imaging was done only for qualitative confirmation of the selective nucleation and growth indicated by fluorescence results. For pattern recognition and equal-concentration experiments, however, shapes in AFM images were uniformly quantified. At least one sample of each of the patterns had three 5 $\times$ 5 µm images taken under comparable conditions. The sample corresponding with each image was blinded, and structures were counted independently by each of the four authors, classifying structures as either "nearly complete" or "clearly identifiable" examples of each of the three shapes. For the purposes of analysing pattern-dependent nucleation and growth, no clear distinction between the number of nearly complete and clearly identifiable shapes was found, and so the two categories were summed. Counts were averaged across the three images, then averaged across the counts of the four authors, to obtain a count per shape per 25 µm$^2$ region for each pattern. Each author used their own, subjective, interpretation of "nearly complete" and "clearly identifiable" structures, and the total number of structures counted in each image differed by up to $\pm$50% for different authors. However, the ratios of different shapes in each image counted by each author remained within 5% of the mean ratios for most images, and across all images, no author had a bias of more than $\pm$4% toward identifying a particular shape more or less often than average.

To measure the selectivity of patterns, the fraction of on-target shape growth time, and AFM counts, compared to the sum of shape growth times and AFM counts, was used. The total growth times, and total AFM counts, of the on-target shapes were used to measure overall shape growth.

**Pattern recognition training.** Images for pattern recognition were selected from several sources, rescaled to 30 $\times$ 30, discretized to 10 grayscale values, and adjusted so that the number of pixels with each value was consistent across all images (see Supplementary Information and Data Appendix, Section 1.6 for details). Each pixel's grayscale value, $0 \leq p_n \leq 1$, was converted to the concentration $c_i$ for the corresponding tile $t_i$ using an exponential formula, $c_i = ce^{3\, p_n \ln 3}$, where the base concentration is $c = 16.67$ nM. The intention of the numbers used was to make the average tile concentration 60 nM for each image. As each image had 900 pixels and there are 917 tiles in the system, 17 tiles did not have their concentrations set by any pixel; these tile concentrations were uniformly set to the lowest concentration, and the assignment of these tiles was used to ensure that fluorophore label locations did not vary in concentration.

The tile-pixel assignment was optimized through a simple hill-climbing algorithm, starting from a random assignment, where random modifications to the assignment map are attempted at each step and accepted if the move increases the efficacy of the map. This efficacy was quantified through a heuristic function that accounts for relative nucleation rates, location of nucleation sites (with emphasis given to locations that succeeded in the flag experiments shown in Fig. 4d), and satisfaction of constraints related to the fluorescent reporters. Because the nucleation algorithm described above is costly, a simplistic model of nucleation based upon the Boltzmann-weighted sum of concentrations over a $k \times k$ window swept over each structure (similar to the model employed in Zhong et al[24]) was used to evaluate relative nucleation rates for a majority of the optimization steps. The more detailed but computationally costly model described above was then employed for an additional several hours in hopes of improving the mapping. The window-based nucleation model (along with all constraints about nucleation location and fluorescent reporters) is also employed to explore the capacity of this map training procedure in Extended Data Fig. E7. Details of the pattern recognition training and the window-based nucleation model are discussed in Supplementary Information and Data Appendix, Sections 1.4 and 1.5.

## References


57. Marras, A., Zhou, L., Su, H. J. & Castro, C. E. "Programmable motion of DNA origami mechanisms". *Proceedings of the National Academy of Sciences* **112,** 713–718 (2015) (cit. on p. 10).

58. Winfree, E. *Self-healing tile sets*. in *Nanotechnology: Science and Computation* (eds Chen, J., Jonoska, N. & Rozenberg, G.) (Springer Berlin Heidelberg, Berlin, Heidelberg, 2006), 55–78 (cit. on pp. 10, 14).

59. Winfree, E. *Simulations of computing by self-assembly*. Tech. rep. CaltechCSTR:1998.22 (Pasadena, CA, 1998) (cit. on pp. 10, 16).

60. Evans, C. G. & Winfree, E. "Physical principles for DNA tile self-assembly". *Chemical Society Reviews* **46,** 3808–3829 (2017) (cit. on pp. 10, 16).

61. Allen, R. J., Warren, P. B. & Ten Wolde, P. R. "Sampling rare switching events in biochemical networks". *Physical Review Letters* **94,** 018104 (2005) (cit. on p. 10).

62. You, Y., Tataurov, A. V. & Owczarzy, R. "Measuring thermodynamic details of DNA hybridization using fluorescence". *Biopolymers* **95,** 472–486 (2011) (cit. on p. 11).

63. Evans, C. G., Schulman, R. & Winfree, E. *The Xgrow Simulator.* https://github.com/DNA-and-Natural-Algorithms-Group/xgrow (cit. on p. 15).

64. Schulman, R. & Winfree, E. "Programmable control of nucleation for algorithmic self-assembly". *SIAM Journal on Computing* **39,** 1581–1616 (2009) (cit. on p. 16).

**Acknowledgements.** We thank Michael Brenner, Aaron Dinner, David Doty, Deborah K. Fygenson, Stanislas Leibler, Richard M. Murray, Lulu Qian, Paul W. K. Rothemund, Chris Thachuk, Grigory Tikhomirov, Damien Woods, and Zorana Zeravcic. Ting Zhu, Thomas Ouldridge, Salvador Buse, Matthew Alexander, Mohini Misra, Anna Lapteva also provided valuable feedback on early drafts.

**Funding.** Supported by National Science Foundation grants CCF-1317694 and CCF/FET-2008589, the Evans Foundation for Molecular Medicine, European Research Council grant 772766, Science Foundation Ireland grant 18/ERCS/5746, and the Carver Mead New Adventures Fund. JOB, AM were primarily supported by the University of Chicago Materials Research Science and Engineering Center, which is funded by National Science Foundation under award number DMR-2011854. AM acknowledges support from the Simons Foundation.

**Author Contributions.** CGE, EW, AM conceived the study. CGE and EW designed the molecules. CGE, JOB, EW, AM wrote simulation code, designed the experiments and performed the experiments, analyzed the data and wrote the manuscript.

**Competing Interests.** The authors declare that they have no competing financial interests.

**Correspondence.** Correspondence should be addressed to cge@dna.caltech.edu, jdobrien@uchicago.edu, winfree@caltech.edu, or amurugan@uchicago.edu.

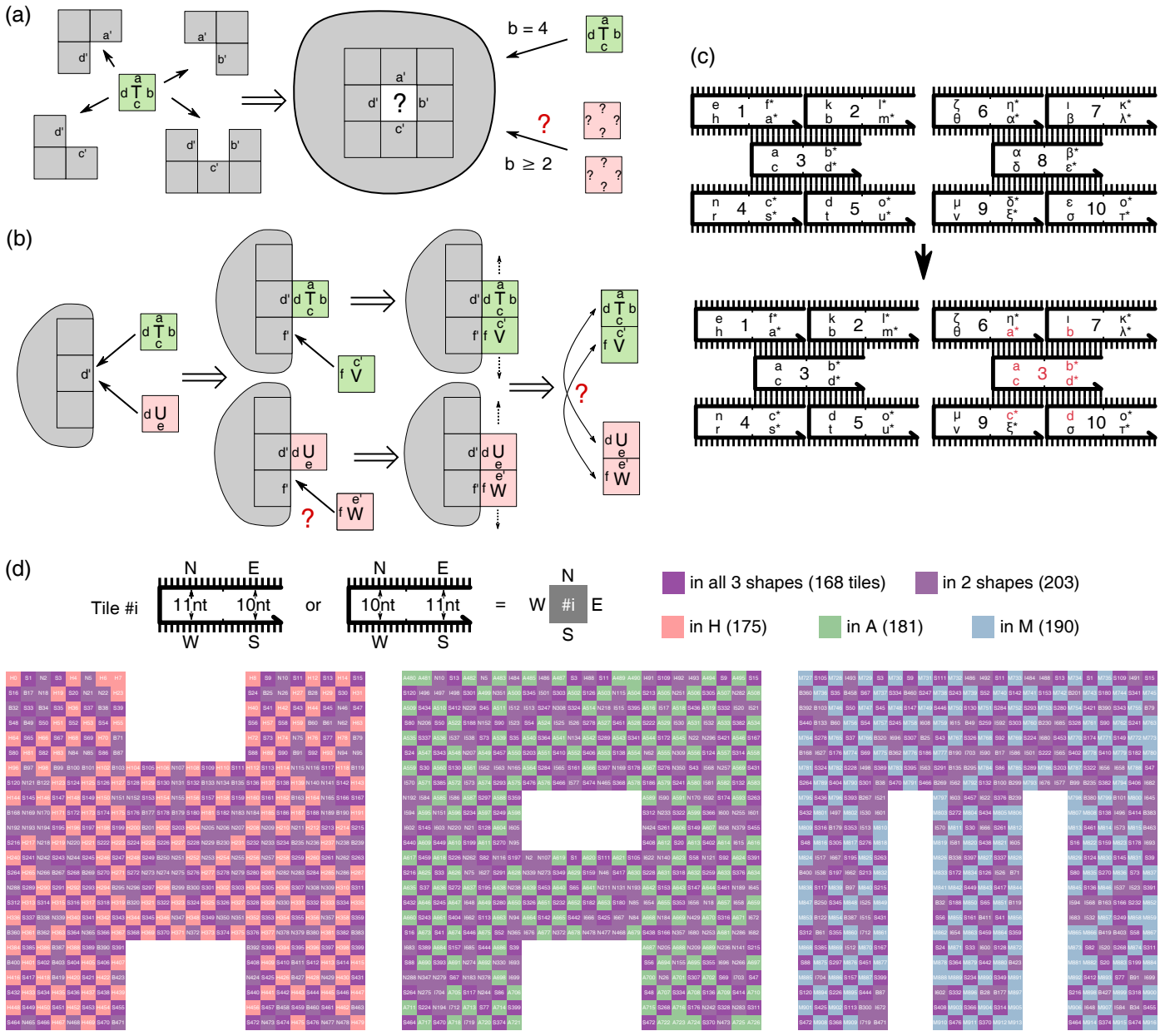


**Fig. E1** | **Proofreading tile set design and tile assignment map. a,** Our systems are designed to grow in a regime where a tile attaching by at least two bonds is favorable, but a tile attaching by one bond is not ('threshold 2'). Motivated by self-healing tile systems,[58] we seek a tile set where no correct partial assembly should ever allow an undesired tile to attach by two or more bonds, though undesired attachments by one bond are allowed, such that any favorable attachment to a partial assembly will be correct. **b,** In addition to tiles attaching favorably by 2 bonds to growing facets, new facets in the system will only be created by tiles attaching unfavorably by one bond, and then being stabilized by further, favorable growth. At a site where tile $T$ would correctly attach by one bond, a tile $U$ might be able to attach incorrectly by the same bond. $T$ would correctly be stabilized by the subsequent attachment of $V$ by two bonds, but $U$ might be able to be stabilized as well if there is a tile $W$ that can attach to it and shares the same glue as $V$. Thus, if for every pair of tiles that can bind to each other (e.g., $T + V$), there is no other pair of binding tiles (e.g., $U + W$) that share two glues on the same edges of the tiles, then any tile that attaches by one bond to an assembly will either be the correct tile, or will not allow a subsequent attachment, and will likely detach. This is equivalent to 'second-order sensitivity' with all directions treated as inputs, functioning as a form of 'proofreading'.[37,38] **c,** We created a multifarious tile system by first starting with three shapes constructed entirely of unique tiles, then repeatedly attempting to 'merge' tiles in different shapes by constraining the sequences of their domains to be identical, and checking whether each merge of two tiles results in a tile system that does not have any tile pairs violating criteria in **a** and **b**. **d,** From multiple trials of the merging process, each initially favoring a checkerboard arrangement before attempting more general merges, we selected the smallest result containing 917 tiles. Tiles in the system were designed with the single-stranded tile (SST) motif,[33] with two alternating tiles motifs of 11 nt and 12 nt domains (tile sequences and full shape layouts are shown in Supplementary Information and Data Appendix, Section 3).

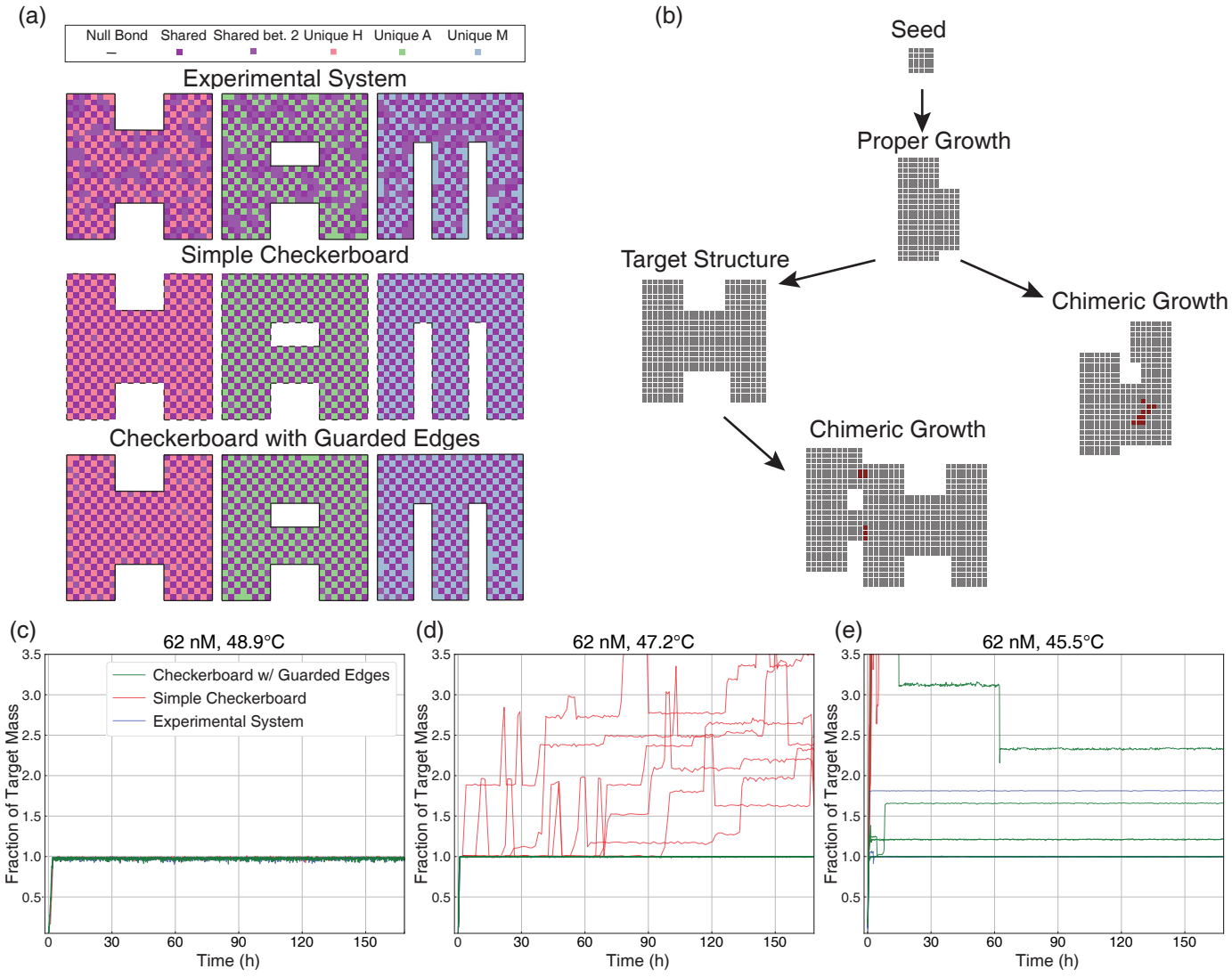


**Fig. E2 | Suppression of chimeric growth through tile set design. a,** We use simulations to contrast assembly errors in three distinct tile sets: the proofreading tile set with an inert boundary used in experiments, described in Fig. 2 **(a, top)**; a simple checkerboard tile set with a strictly alternating shared and unique tile pattern for each shape, where unique tiles can be seen as mediating different interactions between shared tiles **(a, middle)**; and an edge-guarded checkerboard in which we additionally enforce inert bonds around each shape's perimeter **(a, bottom)**. For each tile set, we performed kinetic growth simulations, starting from a pre-formed $5 \times 5$ seed taken from a location within H. Simulations were performed using the kinetic Tile Assembly Model as implemented by XGrow (with chunk fission)[63] with uniform tile concentrations corresponding to 62 nM and parameters estimated in Supplementary Information and Data Appendix, Section 1.1. **b,** Schematic shows the two distinct kinds of chimeric structures (e.g., part-H, part-A) seen in simulation due to promiscuous interactions; chimeric structures can grow either before full assembly of the target structure or emerge spontaneously from the edge of a properly formed structure. Chimeras like those illustrated along the lower path are held together by just a few bonds and sometimes can quickly break apart (tiles with unintended bonds are shown in red): these result in sharp drops in simulated assembly size, as the simulation discards one subassembly when disconnected. **c–e,** The size of the assembly (in units of the size of the fully formed H) is shown as a function of time. For higher temperature 48.9 °C (**c**), no chimeras are observed on the simulated timescales for any tile set. For intermediate temperature 47.2 °C (**d**), all 6 checkerboard trajectories still result in chimeras, while no errors are observed on the timescale probed for the guarded checkerboard or experimentally-implemented proofreading tile set. For lower temperature 45.5 °C (**e**), chimeras are seen in all runs for checkerboard structures (red traces), 4 of the 6 runs for guarded checkerboard structures (green traces) and 1 of the 6 runs for proofreading structures.

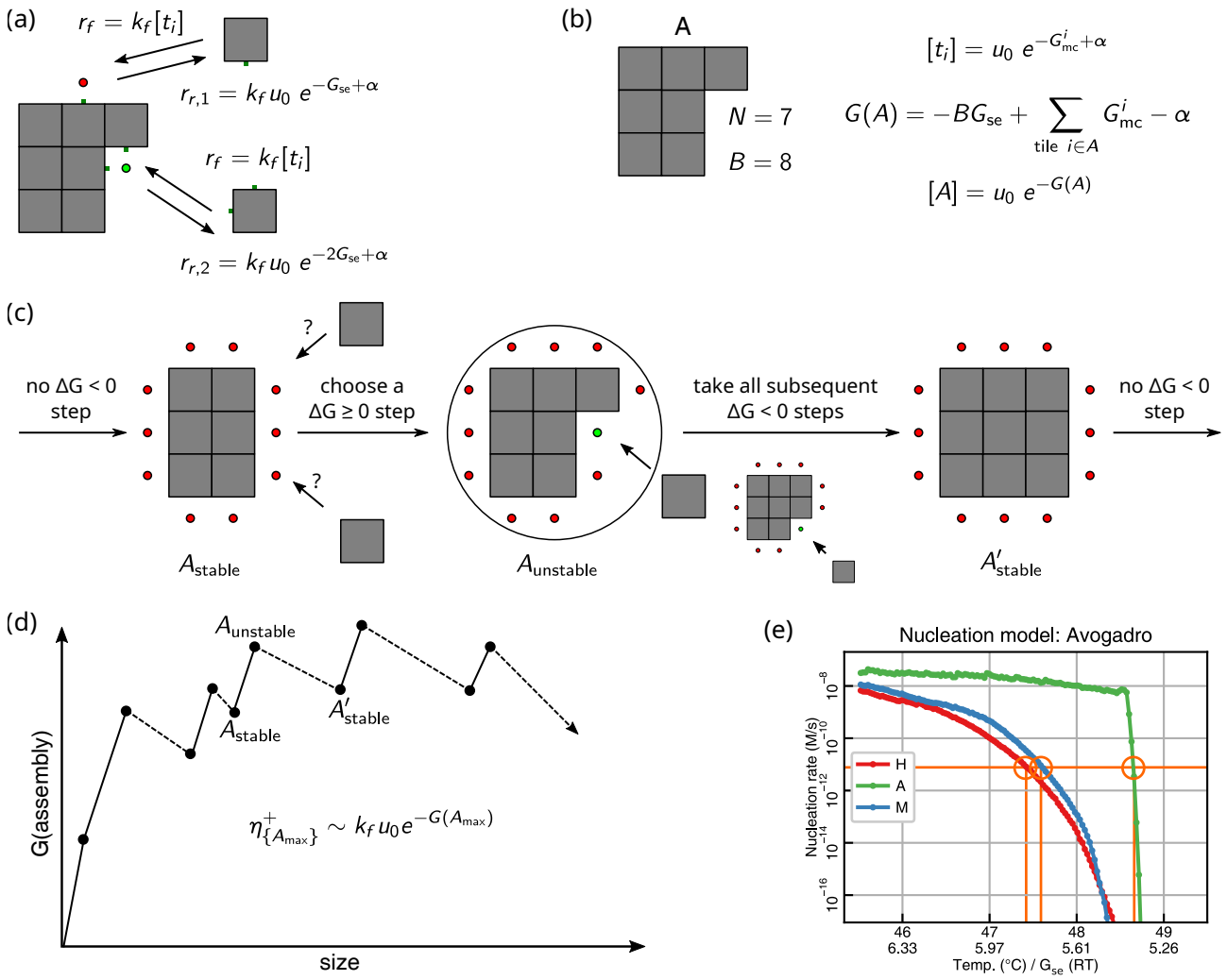


**Fig. E3 | Stochastic Greedy Nucleation Model, based on repeated stochastic simulations. a,** The frequently-used kinetic Tile Assembly Model (kTAM)[59,60] has rates for tile attachment and detachment events based on tile and assembly diffusion and total binding strength of correct attachments a tile can make at a lattice site. Here $u_0 = 1$ M. **b,** These rates can be used to derive a free energy for any tile assembly in a system, and, assuming fixed monomer concentrations, an equilibrium concentration for any assembly. Schulman & Winfree[64] showed that the equilibrium concentration of the highest-energy assembly along a nucleation trajectory under this assumption provides an upper bound for nucleation rate through that trajectory, with or without fixed monomer concentrations. However, in a large system, considering all possible intermediate assemblies and all pathways, including many that are extremely unlikely, would be infeasible. Thus, we developed the Stochastic Greedy Nucleation Model to generate stochastically-chosen paths of tile attachments. **c,** Starting from a single tile (chosen with probability proportional to relative concentration), whenever the assembly is in a state $A_{\text{stable}}$ where there is no tile attachment that would be favorable (have $\Delta G < 0$), one of the possible unfavorable (with $\Delta G \geq 0$) attachments is stochastically chosen, resulting in a higher-$G$ state $A_{\text{unstable}}$. Then, all subsequent possible $\Delta G < 0$ attachments are made, resulting in the next $A'_{\text{stable}}$ state; for our system of unique tiles for each site in the lattice, this sequence of favorable steps has a unique resulting assembly. **d,** The process repeats until all tiles in a shape are attached, which results in a trajectory with a maximum-$G$ assembly that can be used to bound the rate of nucleation, $\eta^+$, through that particular trajectory. **e,** By using this process to collect many trajectories, and then repeating the entire process for each of the three shapes in the system, we can estimate nucleation rates dependent upon temperature, with the assumption that tile monomer concentrations do not deplete, and that the trajectories found are a reasonable representation of likely trajectories. For comparison between model predictions and experimental data in Extended Data Fig. E5d and E8b, we determined the temperature at which the model predicted the nucleation rate exceeded a threshold (orange line), to compare with when fluorescence quenching exceeded a threshold. For more details on the model, see Supplementary Information and Data Appendix, Section 1.2.

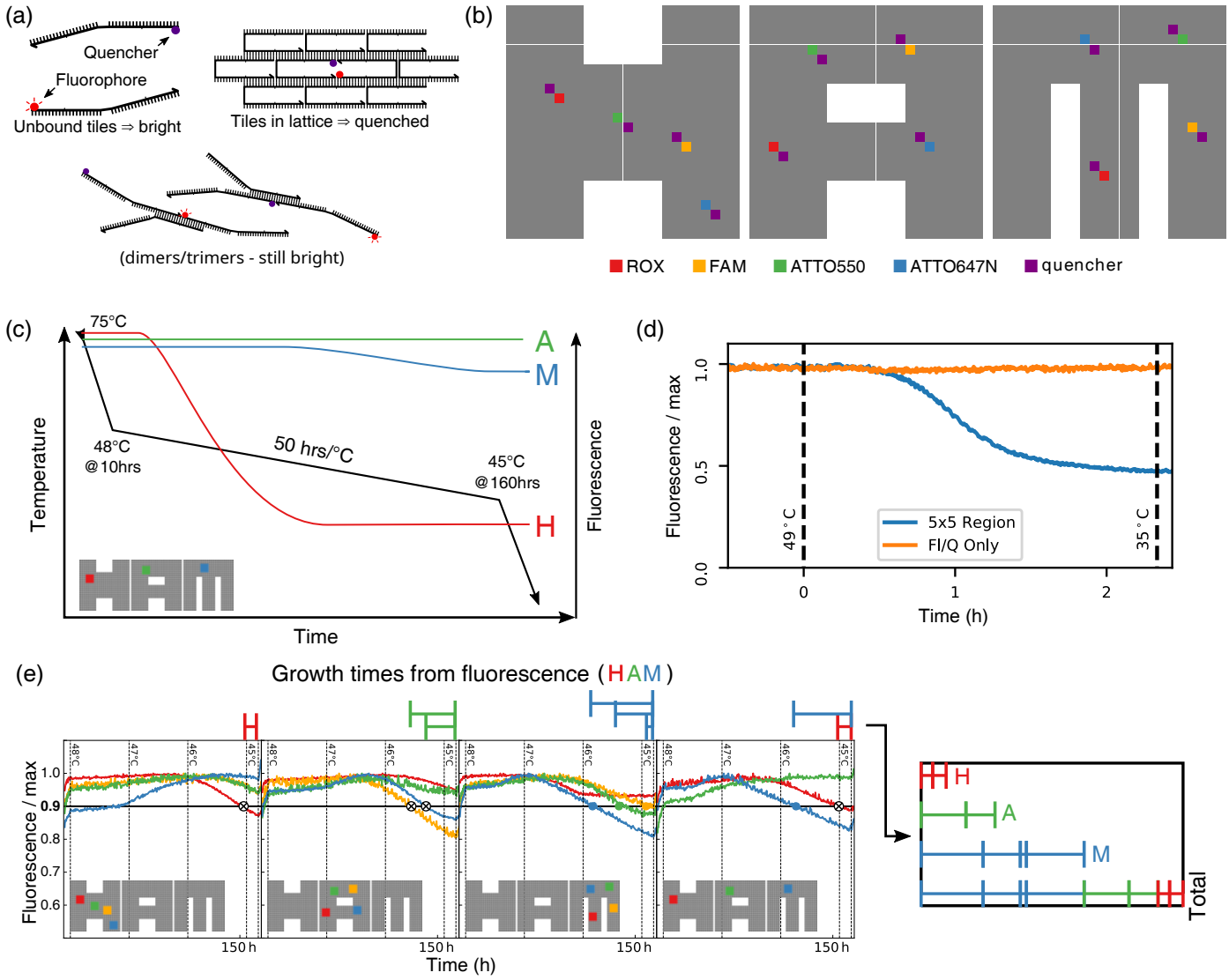


**Fig. E4 | Fluorophore quenching as a measure of nucleation and growth. a,** Fluorescent labels used a fluorophore-quencher pair placed on the 5′ ends of two modified tiles unique to one shape, where they were co-located, but had no complementary binding domains, ensuring that dimers could not form, and trimers would not closely co-locate the fluorophore and quencher. To constrain the pair to be close enough to quench in a well-formed lattice, one of the two tiles had its orientation and crossover position swapped compared to the unmodified tile for the location. **b,** Positions and types of all fluorophore/quencher pairs available for use. For one sample, one position for each of four types of fluorophores could be chosen, and tile pairs for those locations replaced by their modified counterparts. Thus different samples could probe different arrangements of up to four locations; four arrangements were used in experiments (e.g., in **e**). **c,** Expected behavior of fluorophore labels on shapes as one shape nucleates and grows. **d,** Fluorescence data for non-quenching (fluorophore tile only, orange) and quenching ($5 \times 5$ lattice around fluorophore and quencher tiles, blue) controls for the ATTO647N fluorophore/quencher pair on A. Here, the temperature ramps linearly from 49 °C to 35 °C at a rate of 0.1 °C/min, with all tiles at 50 nM, and each sample has its fluorescence normalized to its maximum value independently. **e,** An example of fluorescence growth time measurements (Mockingbird; see Supplementary Information and Data Appendix, Section 5.4.9). Each fluorophore signal, in each sample, is independently normalized to its maximum value during the experiment, and the time between the point where the signal goes below 0.9 ("10% quenching") and the end of the experiment is measured ("growth time"). These times are then summed for all fluorophores, in all four samples, on each shape, resulting in a growth time for each shape, and, when normalized to the sum of all growth times, a relative growth time for each shape. See Methods and Supplementary Information and Data Appendix, Section 2 for design and characterization of fluorophore readout.

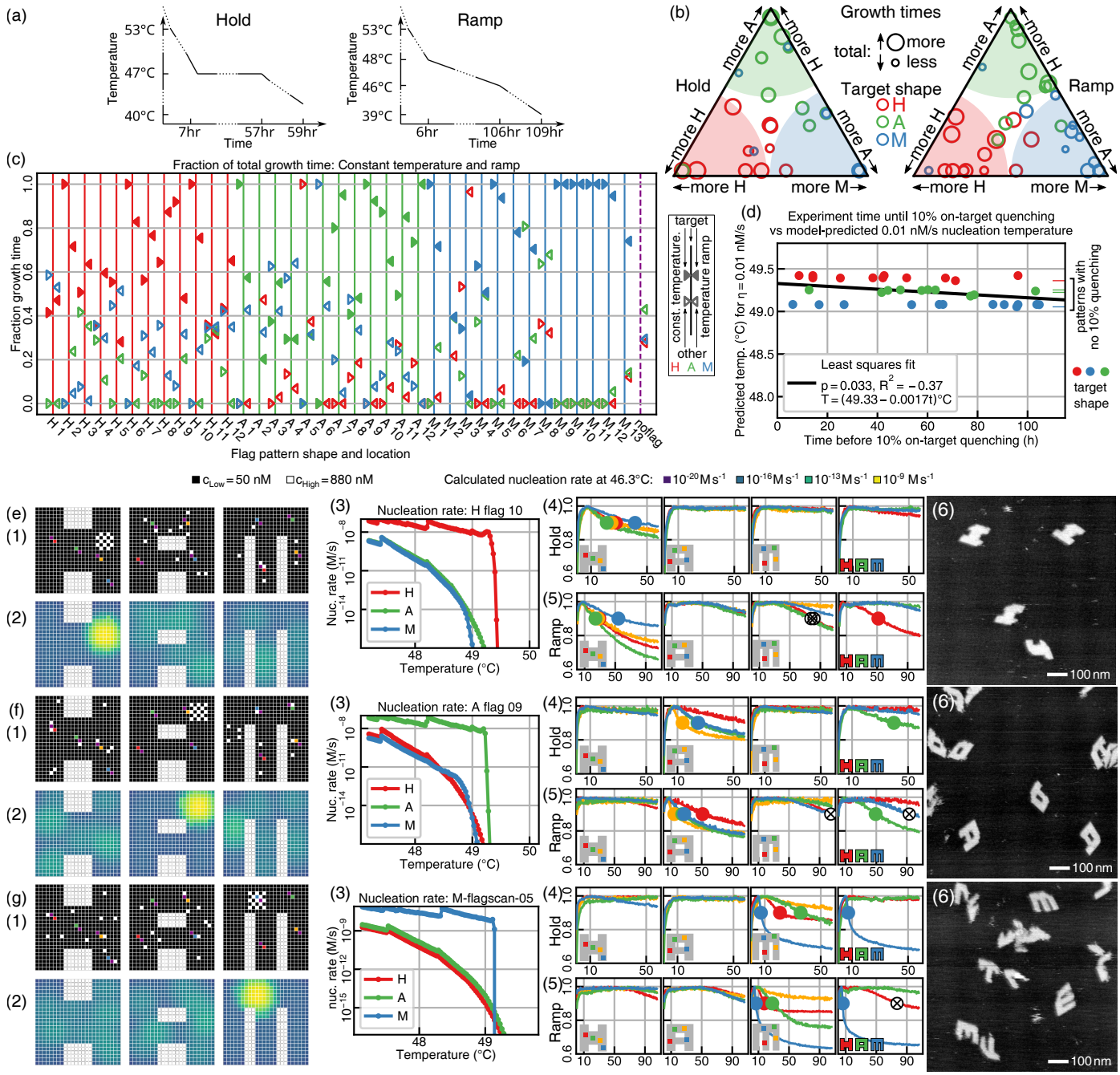


**Fig. E5 | Nucleation and growth with 'flag' patterns of enhanced concentration. a–c,** 36 different concentration patterns with enhanced concentrations of shared tiles in 5 × 5 regions were prepared, each with four different standard sets of fluorophores in four samples, and grown using two temperature protocols (**a**): a ramp focusing on 48 °C to 46 °C over 100 hours, and a hold at 47 °C. Using growth times as described in Extended Data Fig. E4, fluorescence data for many samples in both experiments showed preference for the desired shapes (**b, c**), but with considerable variation in selectivity and total amount of growth. **d,** No statistically significant correlation was found between the nucleation model prediction for temperature of on-target nucleation and the time of on-target shape quenching in the temperature ramp experiment. **e–g,** Details of three patterns, with concentration patterns (1), weighted critical nucleus free energy starting from particular tiles (2), nucleation-model-estimated nucleation rates (3), temperature hold (4) and temperature ramp (5) experiment fluorescence results, and (6) AFM images from the temperature hold experiments. Information for all individual flag patterns is available in the Supplementary Information and Data Appendix, Section 4.

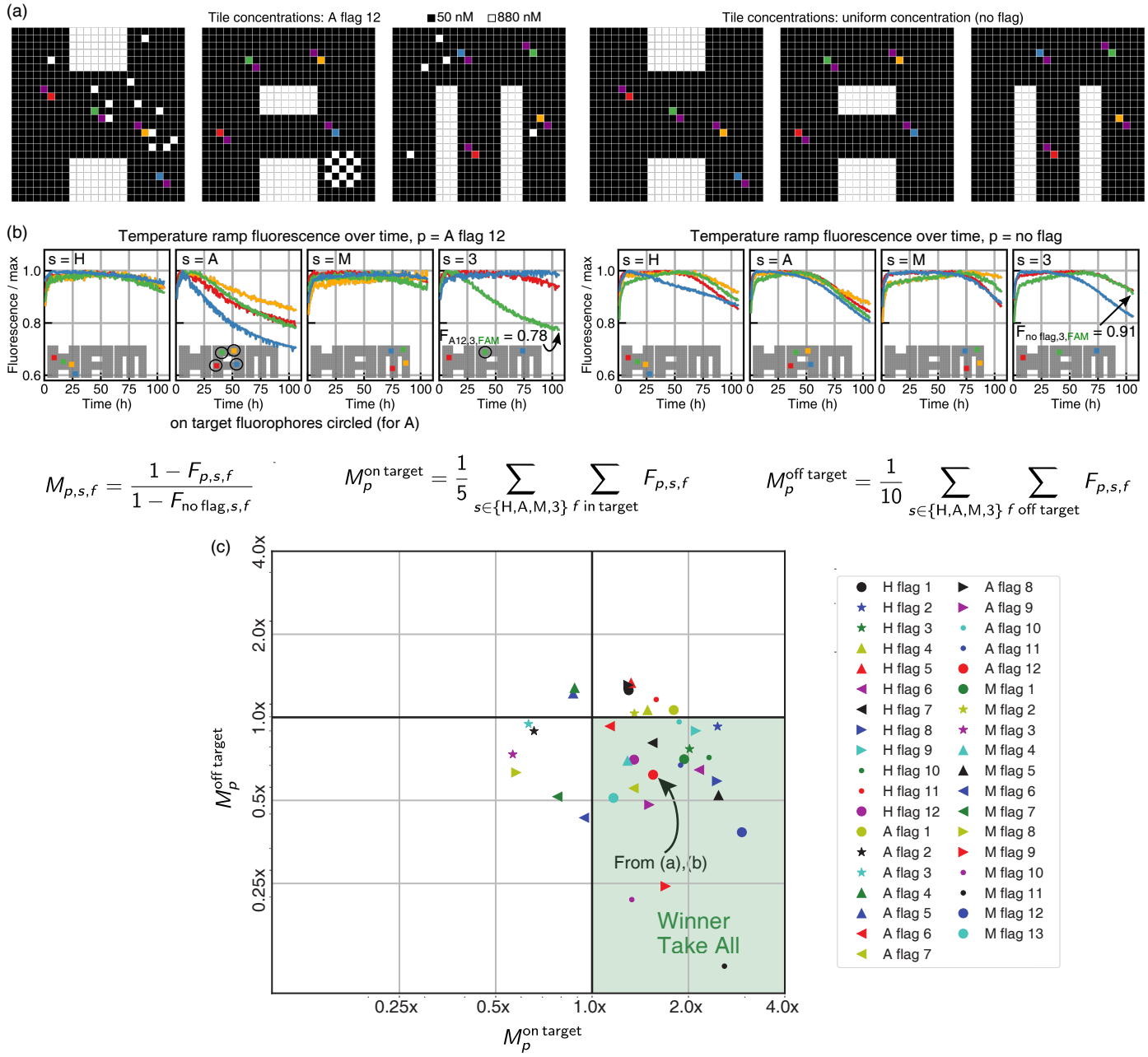


**Fig. E6 | Evidence of winner-take-all in flag experiments. a,** An example flag pattern (A flag 12), and uniform 50 nM concentration 'no flag' pattern. **b,** Fluorescence normalized to maximum readings, from the temperature ramp experiment (Extended Data Fig. E5 and Supplementary Information and Data Appendix, Section 4). The fluorescence at the end of the experiment, $F_{p,s,f}$, of fluorophore $f$ in sample $s$ of pattern $p$ is used along with the value for the corresponding fluorescence value for the no flag pattern, $F_{\text{no flag},s,f}$, to calculate the ratio $M_{p,s,f}$. This ratio corresponds to the relative amount of quenching for that fluorophore in the flag pattern compared to the no flag pattern. The ratios are averaged across the 5 on-target fluorophores (circled in **b**) in samples for the flag pattern to obtain an average on-target ratio, and across the 10 off-target fluorophores to obtain an average off-target ratio. **c,** The on- and off-target ratios are plotted for each flag pattern. For winner take all behavior, on-target quenching is expected to be higher with a flag pattern than with no flag, resulting in $F_p^{\text{on target}} > 1$, while off-target quenching is expected to be reduced, resulting in $F_p^{\text{off target}} < 1$.

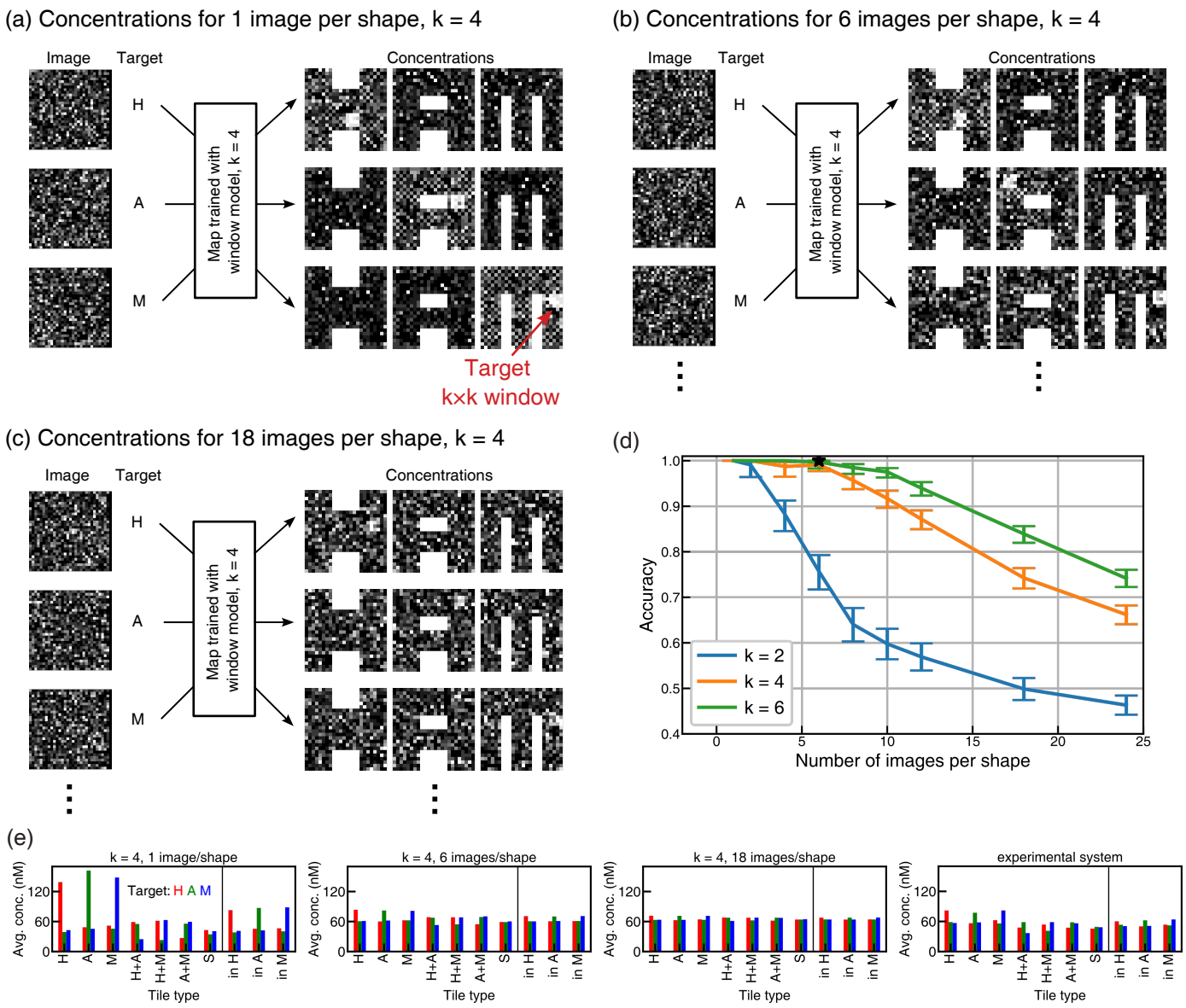


**Fig. E7 | Pattern recognition capacity.** To analyze the pattern-recognition capabilities of the designed tile set, the map-training algorithm (see Supplementary Information and Data Appendix, Section 1.4) was run for increasingly larger sets of random images. **a-c,** Example images mapped to concentration patterns for sets with 1, 12, and 18 trained images per shape, with the intended target shape for each image indicated. Following the same procedure as used for the experimental system, with the same weighting of locations, $30 \times 30$ images with 10 possible grayscale values and matching histograms were mapped exponentially to tile concentrations in the 917 tile system; however, all images were generated randomly. Training was done using only the Window Nucleation Model with a window size $k$ of either 2, 4, or 6, with a limit of 400,000 steps (Supplementary Information and Data Appendix, Section 1.5). For each number of images per shape considered, ten repetitions of training (starting from random assignments) were performed (to account for variability of the training algorithm) for each of three different sets of images (to account for variability in sets of images). **d,** As the number of images in the set increases, the performance of the training algorithm decreases. For larger $k$, the pixel-tile map can exploit higher-order correlations and can thus accommodate more images. For each system, nucleation rates were calculated using the Stochastic Greedy Model, described in Supplementary Information and Data Appendix, Section 1.2, at $G_{se} = 5.4$, which roughly corresponds to a temperature of 48.6 °C, and with concentrations comparable to the experimental system. Specificity was calculated as the nucleation rate of the target shape for each image divided by the total nucleation rate of all three shapes for that image, averaged over all images in the system, and over all 30 systems (10 repetitions for each of 3 sets of images) for each point, with 90% confidence intervals shown. Star shows specificity calculated from nucleation model results for the experimentally-implemented system. **e,** As the number of images increases, pattern recognition must increasingly rely on patterns of concentrations of shared tiles, rather than choosing a pixel-to-tile map that places high-concentration pixels on tiles unique to the target shape. Histograms show average concentrations of tiles in different shapes or combinations of shape (including the average across tile categories) for images in training cases **a–c**, and the experimental system. The change can also be seen in the concentration maps of **a–c**, with the sharp checkerboard of high concentration tiles in target shapes in **a** becoming less apparent in **b** and **c**.

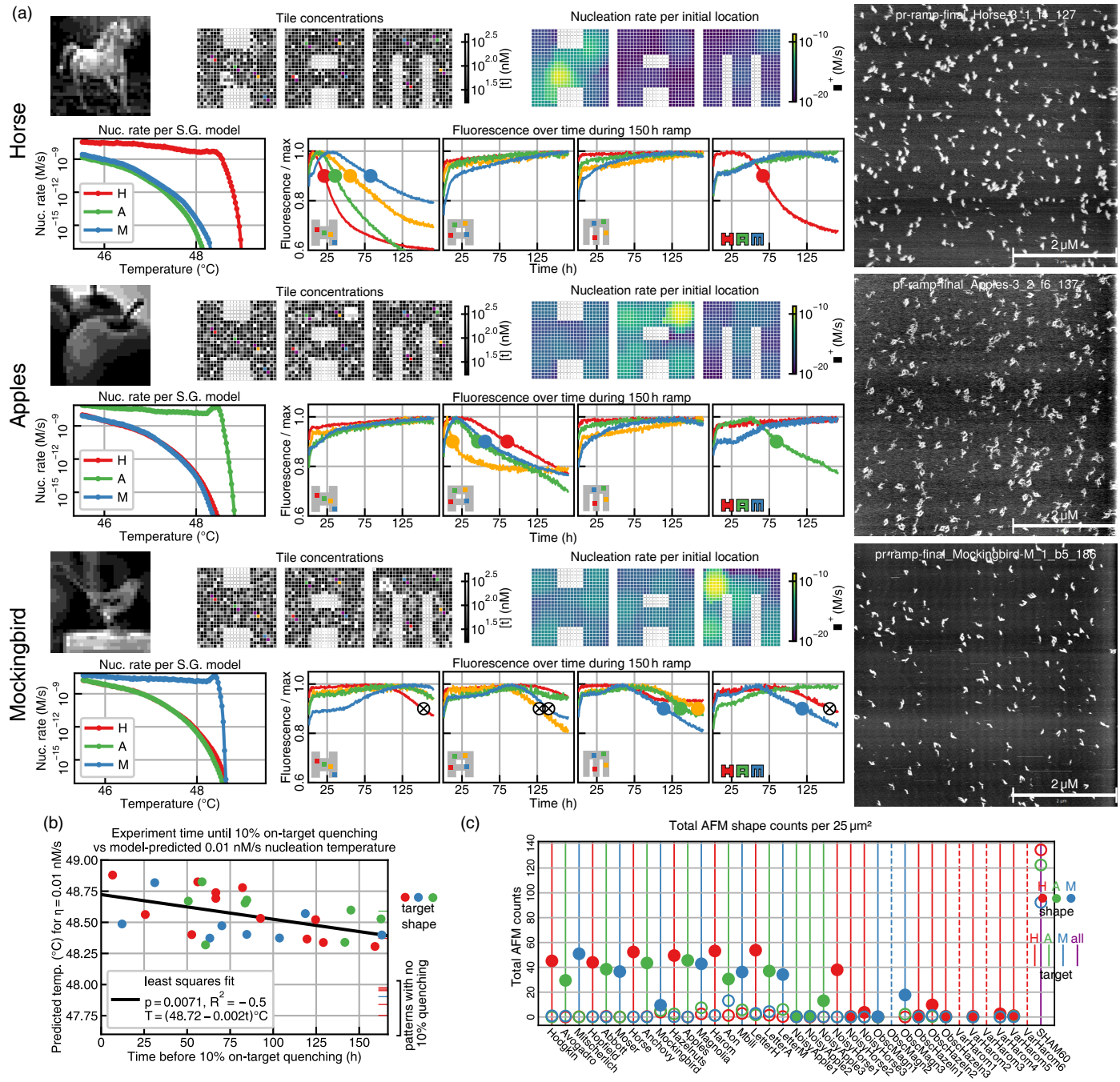


**Fig. E8 | Classification of images viewed as concentration patterns.** 36 different concentration patterns, derived from a mapping of 36 grayscale images, were run using a ramp between 48 °C to 45 °C over approximately 150 hours. **a,** Three pattern examples, with source image, concentration pattern, nucleation model nucleation rate starting from particular tiles, nucleation model nucleation rates, fluorescence results, and AFM images. **b,** Across all patterns there was some correlation between the on-target nucleation temperature predicted by the nucleation model and on-target shape quenching time. **c,** Total AFM shape counts for each sample. Information for all patterns is available in the Supplementary Information and Data Appendix, Section 5.